J. Fluid Mech. (2025), *vol.* 1016, A59, doi:10.1017/jfm.2025.10414

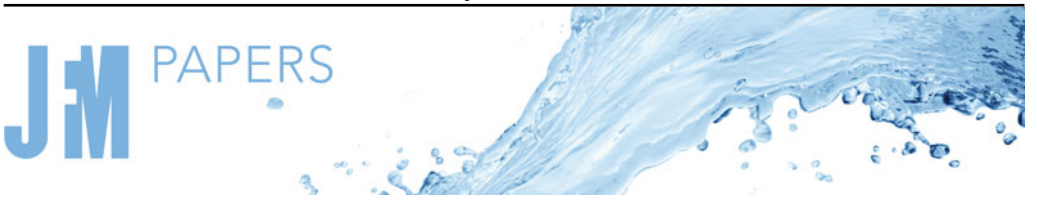

Active control of transition to turbulence in laminar separation bubbles

David Borgmann[1], **Jesse Little**[2] **and Hermann Fasel**[1]

[1]Department of Aerospace and Mechanical Engineering, The University of Arizona, Tucson, AZ 85721, USA

[2]Department of Mechanical and Aerospace Engineering, The Ohio State University, Columbus, OH 43210, USA

Corresponding author: David Borgmann, davidborgmann@arizona.edu

(Received 22 January 2025; revised 17 May 2025; accepted 20 June 2025)

The impact of two-dimensional (2-D) periodic forcing on transition dynamics in laminar separation bubbles (LSBs) generated on a flat plate is investigated experimentally. Laminar separation is caused by the favourable-to-adverse pressure gradient under an inverted modified NACA 64_3-618 and periodic disturbances are generated by an alternating current dielectric barrier discharge plasma actuator located near the onset of the adverse pressure gradient. Surface pressure and time-resolved particle image velocimetry measurements along the centreline and several wall-parallel planes show significant reductions in bubble size with active flow control. Periodic excitation leads to amplification of the Kelvin–Helmholtz (K–H) instability resulting in strong 2-D coherent roller structures. Spanwise modulation of these structures is observed and varies with the forcing amplitude. Intermediate forcing amplitudes result in periodic spanwise deformation of the mean flow at large wavelength ($\lambda_z/L_{b,5kVpp} \approx 0.76$). For high-amplitude forcing, the spanwise modulation of the mean flow agrees with the much smaller wavelength of the difference interaction of two oblique subharmonic modes ($\lambda_z/L_{b,5kVpp} \approx 0.24$). Modal decomposition shows nonlinear interaction of the forced 2-D mode leading to growth of subharmonic and harmonic content, and the observation of several half-harmonics ($[n+1/2]f_{AFC}$) at intermediate forcing amplitudes. Strongest amplitudes of the 2-D mode and delay of transition downstream of the time-averaged reattachment are observed for the intermediate forcing amplitudes, previously only observed in numerical simulations. Consistent with numerical results, further increase of the forcing amplitude leads to rapid breakdown to turbulence in the LSB. This suggests that the most effective exploitation of the K–H instability for transition delay is connected to an optimal (moderate) forcing amplitude.

Key words: boundary layer separation, instability control, transition to turbulence

1. Introduction

In low-Reynolds-number flows, a laminar boundary layer will separate when the adverse pressure gradient is strong enough. When free-stream turbulence (FST) in the incoming flow is low, the hydrodynamic instability of the inviscid shear layer in the separated region governs the flow dynamics and causes a rapid formation of spanwise-coherent vortical structures (see e.g. Rist & Maucher 1994; Diwan & Ramesh 2009; Postl, Balzer & Fasel 2011; Balzer & Fasel 2016; Hosseinverdi & Fasel 2018). Spanwise deformation of these structures (e.g. Postl *et al.* 2011; Marxen, Lang & Rist 2013; Michelis, Yarusevych & Kotsonis 2018) leads to breakdown to turbulence. The resulting turbulent flow enhances entrainment of high-momentum fluid from the free stream and the flow reattaches to the wall. In a time-averaged sense, the region of recirculating flow between separation and reattachment is called a laminar separation bubble (LSB). The stability of the shear layer and the dynamic behaviour of the LSB are highly sensitive to external disturbances in the flow, i.e. disturbances in the approaching boundary layer and FST. The LSB displacement effects and subsequent turbulent boundary-layer formation can drastically impact the aerodynamic efficiency in practical applications, which include but are not limited to turbo-machinery, laminar airfoils used in wind turbines, uncrewed aerial vehicles and other aircraft. In addition, the highly unstable flow field increases noise emission and structural vibrations. Active control of the topology and dynamics of the LSB holds the prospect of reducing the impact of the unsteady dynamics and could provide a more organised and predictable flow field.

Early investigations of laminar separation bubbles date back to the seminal work of Gaster (1967) and Horton (1968), focused on the bubble topology and bursting behaviour at different Reynolds numbers and pressure gradients. The interest shifted towards various stages in the transition process in more recent experimental studies (Häggmark *et al.* 2001; Diwan & Ramesh 2009; Rodríguez *et al.* 2013; Simoni *et al.* 2017; Yarusevych & Kotsonis 2017; Kurelek, Kotsonis & Yarusevych 2018; Michelis *et al.* 2018). Experiments and numerical studies (Rist & Maucher 1994; Postl *et al.* 2011; Marxen, Lang & Rist 2012; Balzer & Fasel 2016) show the progression of Kelvin–Helmholtz (K–H) instabilities in the separated shear layer, their exponential amplitude growth towards nonlinear interaction and subsequent transition to turbulence (Alam & Sandham 2000; Marxen *et al.* 2013; Hosseinverdi & Fasel 2018, 2019). Small disturbances within the incoming flow, i.e. in the upstream boundary layer and in the FST, were found to amplify the instability waves in the highly unstable shear layer (Marxen *et al.* 2009; Hosseinverdi & Fasel 2018, 2019; Rodríguez *et al.* 2021; Jaroslawski *et al.* 2023). The findings from these investigations indicate that the amplified instability waves rapidly reach large (nonlinear) amplitudes within the separated region, which is followed by periodic shedding of spanwise-coherent (two-dimensional, 2-D) vortical structures (Postl *et al.* 2011; Balzer & Fasel 2016; Istvan & Yarusevych 2018; Hosseinverdi & Fasel 2019). The large-amplitude waves and subsequent spanwise vortical structures facilitate momentum exchange and limit the wall-normal extent of the recirculation region, but are insufficient to cause reattachment. Spanwise modulation of these structures is a result of secondary instability mechanisms (Balzer & Fasel 2016; Michelis *et al.* 2018; Hosseinverdi & Fasel 2019; Kurelek *et al.* 2020; Rodríguez *et al.* 2021). The subsequent breakdown into small-scale turbulence in the LSB results in sufficient entrainment of high-momentum fluid from the free stream to cause reattachment.

Several types of instabilities were found to contribute to the breakdown to turbulence in the later stages of unforced LSBs (Marxen *et al.* 2013): (i) a primary global instability; (ii) a secondary instability occurring either as a subharmonic or a harmonic of the fundamental mode; and (iii) a highly localised instability of the attached boundary layer

(e.g. hairpin vortices). Primary global instabilities require the presence of sufficiently strong reverse flow in the LSB. Theofilis (2011) and Rodríguez *et al.* (2013) suggest that a reverse flow level of 7 %−10 % of the free-stream velocity is required for the presence of a global instability in the LSB. The associated spanwise length scale of this instability is generally of the order of the separated region, or rather the size of the vortex trapped inside the LSB (Rodriguez & Theofilis 2010). Temporal growth of a global instability is able to cause self-sustained transition in LSBs, even in the absence of external disturbances (Hosseinverdi & Fasel 2019; Rodríguez *et al.* 2021). Spanwise length scales of the secondary instabilities (ii) are of similar size to the wavelength of the 2-D vortices developing in the shear layer and therefore much smaller than those related to the primary global instability. Two types of the secondary instability are commonly observed for 2-D vortices in a shear layer, leading to either a spanwise deformation of the spanwise vortices or growth in the stagnation region between a vortex pair (Maucher, Rist & Wagner 2000; Jones, Sandberg & Sandham 2008). The secondary instability in the interaction of two vortices manifests as a subharmonic of the dominant K–H mode in the shear layer. The third type (iii) of instabilities occurs in the presence of localised regions of strong shear in attached boundary layers (Bake, Meyer & Rist 2002), e.g. contributing to the complex formation of hairpin vortices in late stages of the transition in boundary layers.

Contrary to ideal conditions in linear stability calculations and idealised numerical simulations ($Tu = 0\,\%$), flight tests and wind tunnel experiments are never void of FST. Even at low levels, this significantly impacts the transition process in both experiments (Klebanoff 1971; Simoni *et al.* 2017; Jaroslawski *et al.* 2023) and simulations (Jacobs & Durbin 2001; Balzer & Fasel 2016; Istvan & Yarusevych 2018; Hosseinverdi & Fasel 2019; Borgmann *et al.* 2025). At sufficiently low levels of FST ($Tu \lesssim 0.5\,\%$), the shear-layer roll-up remains largely 2-D. For an increased level of FST ($Tu > 0.5\,\%$), streamwise streaks related to Klebanoff modes (Klebanoff, Tidstrom & Sargent 1962; Klebanoff 1971; Kendall 1985; Fasel 2002; Marxen *et al.* 2013; Hosseinverdi & Fasel 2017) appear in the boundary layer, and eventually ($Tu > 1\,\%$) lead to bypass transition (Morkovin 1969; Kendall 1985; Jacobs & Durbin 2001). Even low levels of FST ($Tu = 0.05\,\%$) show a significant reduction in the separation length in direct numerical simulation (Balzer & Fasel 2016). The reduction in bubble size is related to an earlier onset of transition with increasing levels of FST as a consequence of the existing amplitudes of relevant disturbances in the free stream (Hosseinverdi & Fasel 2019; Borgmann *et al.* 2025). The excitation of hydrodynamic instabilities is strongly dependent on the frequency content in the flow, placing particular importance on the spectral content of the FST and not only the integral measure, Tu. However, the spectral content is rarely matched between experiments and simulations.

In conditions of low FST, the entrainment of high-momentum fluid from the free stream and the resulting reattachment have two major contributors: (i) the development of 2-D roller structures resulting from disturbance growth due to the shear-layer instability and (ii) turbulent mixing following the transition process. In the absence of artificial disturbance input, the spanwise-coherent vortices generally do not provide sufficient momentum exchange and reattachment is a result of subsequent turbulent breakdown. Experimental and numerical investigations often introduce small-amplitude disturbances at the most unstable frequencies relevant to the LSB far upstream of separation without changing its time-averaged topology (Alam & Sandham 2000; Marxen *et al.* 2003; Diwan & Ramesh 2009; Kurelek *et al.* 2020), to track the growth and development of naturally occurring disturbances. Marxen & Henningson (2011) found that small (but not too small) forcing amplitudes trigger the laminar to turbulent transition process and cause the appearance of well-organised 2-D vortical structures in the flow similar to the

experimental findings with small periodic disturbance input in Watmuff (1999) and Diwan & Ramesh (2009) using acoustic forcing through a point source upstream of separation. Further increased forcing amplitudes decrease the bubble size and accelerate the transition in the LSB. Contrary to investigating the natural transition by small disturbance input, more recent efforts by Michelis, Yarusevych & Kotsonis (2017) (flat plate) and Yarusevych & Kotsonis (2017) (NACA 0012) focus on the impact of active flow control (AFC). With moderate forcing amplitudes, reduction in bubble size is accompanied by strong 2-D vortical structures. This highlights the receptivity of the instabilities in the LSB to disturbances in the upstream boundary layer.

Extensive numerical simulations applying AFC to the transition process in the LSB have shown the ability to exploit natural disturbance amplification through the K–H instability in the shear layer when forcing near the most unstable frequency of the base flow (Hosseinverdi & Fasel 2019; Yeh *et al.* 2020). Periodic excitation was successful in reducing the separated region (Jones *et al.* 2008; Benton & Visbal 2016; Gross, Little & Fasel 2017), and was able to delay laminar to turbulent transition, or even eliminate it completely (Postl *et al.* 2011; Embacher & Fasel 2014; Hosseinverdi & Fasel 2018). Forcing the primary convective instability strongly amplifies disturbance waves within the K–H frequency range of the separated shear layer. The introduced disturbances grow until they saturate to finite nonlinear amplitudes. The result is observed as strong periodic shedding of spanwise-coherent vortical structures, originating just upstream of the maximum bubble height in the LSB. These large-amplitude waves (or vortices) lead to an exchange of momentum between the LSB and the free stream, sufficient to cause reattachment without breakdown to turbulence, limiting the extent of the separated region. With optimal choice of amplitude and frequency, Embacher & Fasel (2014) showed that input of 2-D disturbance waves can suppress the secondary absolute instability and thus delay transition and even relaminarise the flow downstream of reattachment. This is fundamentally different from AFC strategies that employ periodic excitation for control of turbulent shear layers (e.g. Greenblatt & Wygnanski 2000) since laminar flow is maintained. In the high-order accurate numerical simulations of Embacher & Fasel (2014), the effects of realistic conditions, such as FST, noise and vibrations, were neglected. Hosseinverdi & Fasel (2018) introduced low-amplitude isotropic FST ($0.0005\,\% \leqslant Tu \leqslant 0.05\,\%$) to the inflow boundary and found that the control was still effective, with transition downstream of the LSB, but closer to reattachment with increasing FST levels. Therefore, the question arises as to whether the observed transition delay and relaminarisation of the flow are still possible in wind tunnel experiments and even free flight conditions.

In this paper, experimental investigations of AFC in LSBs on a flat plate are presented. Two-dimensional periodic forcing near the onset of the adverse pressure gradient was facilitated through an alternating current dielectric barrier discharge (ac-DBD) plasma actuator. The objective of the presented work is to exploit the inherent growth of the K–H instability in the LSB shear layer to (i) increase the maximum amplitude and organisation of the spanwise-coherent vortical structures and the associated entrainment and (ii) influence the transition dynamics and possibly delay the transition to a streamwise location downstream of the mean reattachment location similar to the computations in Hosseinverdi & Fasel (2019). The paper is organised as follows. After a description of the experimental set-up and of the ac-DBD plasma actuator in § 2, a short review of the analysis tools, e.g. spectral proper orthogonal decomposition (SPOD) and bispectral mode decomposition (BMD), is provided in § 3. The results in § 4 show the mean flow topology (§ 4.1) and the influence of forcing on the primary instability (§ 4.2), followed by a discussion of the unsteady behaviour and the nonlinear interactions downstream of linear disturbance growth (§§ 4.3 and 4.4).

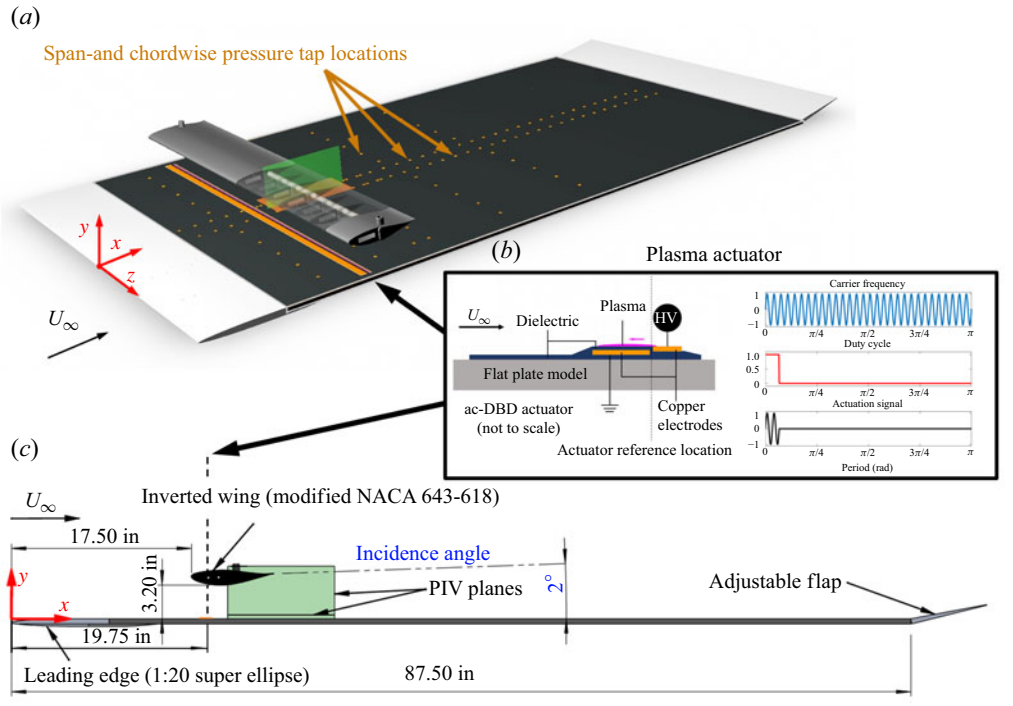

Figure 1. (*a*) Isometric view and (*c*) 2-D schematic of the flat-plate model and inverted wing used for the LSB experiments in ALSWT. Shown are pressure taps and particle image velocimetry (PIV) planes for centreline (green) and wall-parallel (orange) measurements, as well as the actuator location. (*b*) Schematic of the plasma actuator and sample of the voltage trace for pulse generation. Duty cycle superposed on the carrier frequency generates disturbance input with $f_{AFC} = \pi$/period.

2. Experimental set-up and instrumentation

2.1. *Wind tunnel model*

All experiments are performed in the Arizona Low Speed Wind Tunnel (ALSWT) situated in the Department of Aerospace and Mechanical Engineering at the University of Arizona. The closed-loop wind tunnel has a test section of 0.9 m × 1.2 m × 3.65 m (height × width × length, 3 ft × 4 ft × 12 ft). Static and total pressure in the test section are recorded using a Pitot tube mounted 0.4 m downstream of the test section entry at the tunnel sidewall extending into the free stream. Mean flow uniformity is at or better than ±0.5 % and turbulence intensity is measured at $Tu \leq 0.035$ % in the range of 1 Hz to 10 kHz at tested free-stream conditions of $U_\infty = 7\ \mathrm{m\,s^{-1}}$ (Borgmann *et al.* 2021). Free-stream temperature is regulated by a heat exchanger with a chilled water supply and held within the range of ±1 °F (0.44 °C) of 72 °F (22.2 °C) throughout the experiments. Borgmann *et al.* (2020) present a more extensive investigation of the free-stream properties at similar operating conditions. The LSBs are generated on a flat plate by an inverted NACA 64_3-618 airfoil with a chord length of $c = 8$ in. (203.2 mm; see figure 1). Projection of the favourable to adverse pressure gradient along the suction side of the airfoil onto a flat plate neglects the influence of surface curvature on the transition process (Gaster 1967). In this work, the inverted wing is placed at a distance of 3.2 in. (81.3 mm) from the plate surface; 17.5 in. (0.44 m) downstream of the leading edge; at an incidence angle of 2° (relative to the inverted airfoil; see drawing in figure 1). Boundary-layer suction along 50 %−60 %-chord and 85 %−90 %-chord on the suction side and a zigzag turbulator tape

to trip the flow close to the leading edge at the pressure side avoid separation on either surface of the inverted wing (Borgmann *et al.* 2021, 2025). A three-stage vacuum motor (LAMB AMETEK 117500-12) is connected to both ends of the wing, connecting to a PVC pipe with carefully distributed suction holes located inside the plenum of the hollow downstream half of the inverted wing to ensure even suction across the span.

The flat-plate model shown in figure 1 spans nearly the entire width of the test section at 47.75 in. (1.21 m). Gaps between the plate and the test section walls were sealed with a soft expanding foam. The model core is made from an aluminium honeycomb structure, covered on both sides by a 1 mm aluminium skin. The plate is 78 in. (1.98 m) long with a total thickness of 0.5 in. (13 mm) and a flatness of ± 0.008 in. ft^{-1} (± 0.665 mm m^{-1}). Streamlined support structures elevate the flat-plate model to 8.25 in. (210 mm) above the wind tunnel floor to avoid wall effects. The leading edge is a 1:20 super-ellipse (Lin, Reed & Saric 1992) with a length of 9.5 in. (241 mm) and smooth transition to the plate top surface. An adjustable flap at the trailing edge of the plate ensures consistent and repeatable inflow conditions, as it compensates for blockage and allows for positioning of the stagnation point along the leading edge. Flow along the bottom side of the plate was tripped just downstream of the leading edge to reduce unsteadiness in the flow underneath the plate. The origin of the coordinate system used throughout the investigation is located at the centre of the leading edge, with the x axis in streamwise, y axis in vertical and z axis in spanwise direction. The plate surface is considered zero in the vertical (y) direction. All results in this paper are presented in dimensionless form where x and y are scaled with a reference length of $L^*_\infty = 0.0254$ m, which is consistent with scaling used in previous experimental and numerical work for the same model (see Borgmann *et al.* 2025), and follows the early experiments by Gaster (1967).

2.2. *Active flow control*

Forcing of the dominant 2-D disturbance in the LSB shear layer was realised by an ac-DBD plasma actuator (Corke, Enloe & Wilkinson 2010; Benard & Moreau 2014; Kotsonis 2015). The spanwise uniformity of the ac-DBD actuator (Michelis *et al.* 2017; Yarusevych & Kotsonis 2017; Weingaertner, Tewes & Little 2020) provides the desired disturbance input to amplify the 2-D instability in the LSB. The forcing location in this work was chosen at 19.75 in. (0.502 m) from the flat-plate leading edge, just upstream of the onset of the adverse pressure gradient. Other forcing locations were considered in Borgmann *et al.* (2022); however, significant damping of disturbances in the favourable pressure gradient reduces the disturbance amplitude entering the shear layer at laminar separation. To maximise the available range of forcing amplitudes within the physical limitations of the ac-DBD actuator, the forcing was moved as far as possible downstream without any part of the actuator extending into the adverse pressure gradient.

The ac-DBD actuator was built from a 0.05 mm (0.002 in.) Kapton tape base layer (1 in. wide) insulating the actuator from the aluminium plate. A copper tape with a thickness of 0.07 mm (0.0028 in., 0.5 in. wide) was used as the ground electrode and covered by a dielectric layer (Kapton tape, 0.05 mm (0.002 in.), 2 in. wide). The high-voltage electrode (copper tape, 0.07 mm (0.0028 in.), 0.25 in. wide) was placed downstream of the ground electrode on the dielectric layer (figure 1*b*) and is exposed to the flow. The actuation signal consists of a carrier frequency of 3 kHz and a square wave, adjusted in period and width to define the forcing frequency and duty cycle, respectively (figure 1*b*). The forcing frequency is chosen based on stability calculations for the baseline LSB without the actuator in Borgmann *et al.* (2025). From experiments and direct numerical simulations (with near-identical time-averaged flow fields) the centre of a broad

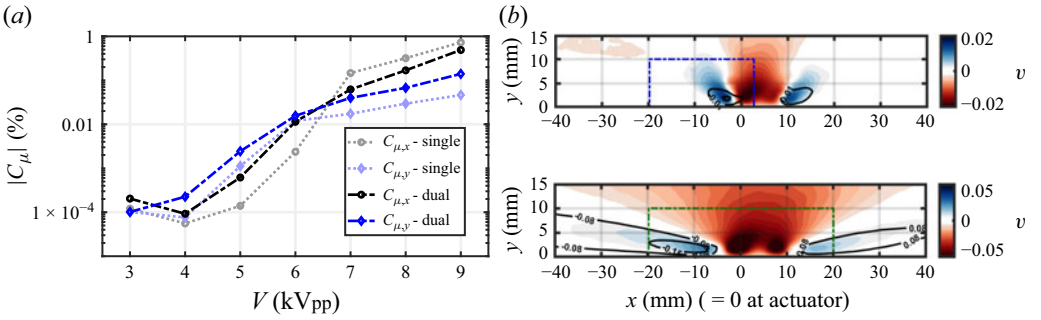

Figure 2. (*a*) Momentum coefficients (C_μ) for the DBD plasma actuator. (*b*) Velocity contours for the u (lines) and v (colours) velocity components of the time-averaged flow field induced by the actuator at 5 kVpp (top) and 8 kVpp (bottom), duty cycle = 13.3 % in quiescent conditions. The dashed line marks the integration domain for the C_μ values shown on the left. The asymmetric domain (blue dash-dotted rectangle, top) encloses the primary AFC pulse facing upstream while the symmetric domain (green dash-dotted rectangle, bottom) captures the entire momentum input.

peak of dominant frequencies in the separated shear layer was found at approximately 250 Hz. Linear stability theory (LST) results in Borgmann *et al.* (2025) have shown that the most unstable frequency is expected at approximately 200 Hz; however, the growth rates remain similar across a wide rage of frequency between 150 and 300 Hz. Preliminary tests varying the forcing frequency (between 185 and 250 Hz) at fixed amplitudes resulted in only very small changes in the mean flow, and caused the periodic structures in the shear layer to 'lock on' to the forced frequency in each case. In addition, stability calculations by Yarusevych & Kotsonis (2017) in a forced LSB show that the forcing frequency does not change the most unstable frequencies in the shear layer, while at increased forcing amplitudes, the most unstable frequency band is slightly lower alongside a decrease in bubble size.

The momentum generated by the actuator depends strongly on the applied peak-to-peak voltage. The voltage at the actuator is measured using a Tektronix P6015 high-voltage probe at the actuator leads. Changes in duty cycle – number of carrier frequency pulses per cycle – did not show a major impact on the flow response in the range surveyed (7 %−50 %). In this study, the actuation is set to two cycles of the carrier frequency at an interval of 5 ms resulting in a duty cycle of 13.3 % at a forcing frequency of 200 Hz at select amplitudes. The amplitudes in this work are referenced by their respective peak-to-peak (pp) voltages between the electrodes of the actuator, e.g. 5 kVpp.

The layout of the actuator results in a plasma discharge in the upstream direction between the high-voltage electrode and the ground electrode. Additionally, measurements of the flow field at the actuator in quiescent conditions show a secondary, weaker discharge between the high-voltage electrode and the aluminium flat-plate surface (figure 2*b*). Similar actuators have been used successfully in previous research on plasma-based flow separation control on airfoils and flat plates (e.g. Corke *et al.* 2010; Michelis *et al.* 2017; Little *et al.* 2019), albeit in a single-discharge configuration when mounted on a non-conductive material. The resulting flow field resembles two opposing wall-parallel jets originating at the actuator accompanied by wall-normal suction in the direction of the high-voltage electrode. These features are significantly different from the forcing input of traditional vibrating ribbon and blowing/suction experiments (figure 2*b*). The developing laminar boundary-layer encounters the plasma-based forcing of the primary discharge before reaching discontinuities from the actuator layout, minimising the geometrical influence of the actuator.

Voltage (kVpp)	$\lvert U\rvert_{max}/U_\infty$ (%)	$\lvert V\rvert_{max}/U_\infty$ (%)	$\lvert C_{\mu,x}\rvert$ (%)	$\lvert C_{\mu,y}\rvert$ (%)
3	0.07*	0.23*	$1.48 \times 10^{-4*}$	$1.02 \times 10^{-4*}$
4	0.10*	0.16*	$1.03 \times 10^{-5*}$	$2.25 \times 10^{-4*}$
5	0.31	0.29	1.07×10^{-3}	2.44×10^{-3}
6	0.93	0.57	6.60×10^{-3}	1.5×10^{-2}
7	1.85	0.94	2.15×10^{-2}	3.9×10^{-2}
8	2.86	1.26	0.11	6.7×10^{-2}

Table 1. Actuator characteristics for quiescent conditions, scaled by the reference free stream in the LSB experiments $U_\infty = 7\ \mathrm{m\,s^{-1}}$; C_μ values are shown for the integral around the dual pulse (figure 2*b*, bottom). ∗Values are of the same order as the PIV uncertainty.

The local flow field in the vicinity of the plasma actuator is examined using planar particle image velocimetry (PIV) measurements in the x–y plane. The small momentum input, especially at low-amplitude forcing, is a significant challenge for the measurement. In previous experimental studies, continuous forcing was used at the actuator carrier frequency to increase momentum input (Maden *et al.* 2013; Michelis *et al.* 2017; Yarusevych & Kotsonis 2017). The momentum input in burst mode is then approximated by scaling the results from continuous forcing with the respective duty cycle. In the current investigation, voltage measurements at the actuator leads show that the peak-to-peak voltages vary between the first and last pulse, with the first pulse (peak-to-peak) in a burst being up to 10 % below that of the following pulses. The present results were therefore recorded in burst mode using identical forcing parameters to those of the AFC applied to the LSBs in § 4. Even though qualitatively the flow field for the lowest forcing amplitudes ($\leq$ 4 kVpp) is very similar to that shown for 5 kVpp (figure 2*b*), the maximum measured velocity magnitudes were small and near the estimated statistical uncertainty of the PIV measurements (using a 95 % confidence interval, 0.01 $\mathrm{m\,s^{-1}}$) (table 1). An asterisk was added to denote the uncertainty on these cases. However, values are provided here for completeness.

Momentum coefficients (C_μ) of the actuator were calculated based on the velocity fields, assuming uniform pressure and 2-D behaviour of the actuator along its entire length (l_{ac}). Calculations use the integration paths shown in figure 2(*b*), following the formulations in Woszidlo & Little (2021) with the time-averaged momentum ($\overline{I}$) over an appropriate control volume boundary (S) following the definition in Kotsonis *et al.* (2011) and Michelis *et al.* (2017):

$$C_\mu = \frac{\overline{I}}{q_\infty l_{ac}} \quad \text{with} \quad \overline{I} = \oint_S \rho_\infty \overline{\boldsymbol{u}}(\overline{\boldsymbol{u}} \cdot \boldsymbol{n})\mathrm{d}S, \tag{2.1}$$

where q_∞ is the dynamic pressure and ρ_∞ the density of the free stream in the LSB experiments.

The magnitude of the momentum coefficients in the x and y directions ($C_{\mu,x}$ and $C_{\mu,y}$) are shown in figure 2(*a*) following the two control volumes shown in figure 2(*b*). Momentum coefficients in x and y increase exponentially as expected for this type of actuator. The C_{mu} values are of the same order of magnitude as those reported in Kotsonis *et al.* (2011) when assuming continuous operation, e.g. correcting for the lower duty cycle in the present work. Figure 2(*b*) shows the time-averaged velocity field of the actuator operated at 5 and 8 kVpp in quiescent conditions. The dash-dotted lines in the two figures highlight the two different integration regions for the C_μ values in figure 2(*a*). The integration domain in figure 2(*b*) (top) captures only the primary plasma pulse between the

high-voltage and ground electrodes, commonly used in previous studies (Michelis *et al.* 2017; Yarusevych & Kotsonis 2017; Weingaertner *et al.* 2020). The symmetric integration domain (figure 2*b*, bottom) captures the entire momentum input by the actuator, and is chosen to capture the entire momentum input by the actuator used in this work (values in table 1 are based on this symmetric domain). It should be noted here that in the low to intermediate forcing amplitudes, the wall-normal momentum input (towards the wall) is higher than the wall-parallel momentum input (≤ 6 kVpp). At high voltages, the primary pulse dominates the flow field and causes a higher streamwise (upstream) momentum input compared with the wall-normal momentum. In the presence of free stream, the total disturbance amplitude input is assumed to stay the same for documentation purposes. However, the direction of the disturbance input likely experiences a significant change with the addition of free stream.

2.3. *Instrumentation*

Surface pressure is measured via pressure taps located along two lines in the streamwise direction, 1.5 in. (38 mm) to either side of the centreline (figure 1). The streamwise spacing is 0.5 in. (12.5 mm) in the vicinity of the LSB and 1 in. (25 mm) elsewhere. The pressure tap spacing is gradually refined towards the leading edge with the first tap at 0.6 in. (15 mm) from the leading edge and an initial spacing of 0.2 in. (5 mm). Time-averaged pressure was measured using Scanivalve Corp. ZOC33 pressure scanners (with a full scale (FS) range and accuracy of FS = 2.49 kPa (10 in. H_2O) $\pm$ 0.15FS) in combination with an ERAD Remote A/D module. Data were sampled until a relative statistical uncertainty of $< 1\,\%q_\infty$ (or 0.16 % FS (2.49 kPa)) was reached within a 95 % confidence interval, leading to a combined systematic and statistical uncertainty of 0.22 % FS (2.49 kPa).

Time-resolved PIV was recorded using a LaVision GmbH stereoscopic PIV system to obtain spatially resolved velocity data along the centreline of the wind tunnel ($x-y$ plane) and several wall-parallel $x-z$ planes in the range 2 mm $\leq y \leq$ 10 mm. Diethylhexyl sebacate seed particles were illuminated by a Photonics DM1-527-50 Nd:YLF laser and images were recorded using two Phantom Ultra High-Speed Cameras v2012, in parallel for 2-D PIV in the $x-y$ plane and in a stereo configuration for all other planes, placing both cameras on either side of the wind tunnel ceiling facing the flat-plate surface. Sampling rates for the image pairs are set to 1197 Hz. The full frame of the 1 megapixel sensor (1260 px $\times$ 800 px) was used in the wall-parallel planes, while the field of view was reduced in the $x-y$ plane, increasing the number of samples per recording. Each camera was equipped with a teleconverter and a 50 mm lens incorporating a scheimpflug mount in the stereo configuration. Image pairs were pre-processed using background subtraction via a high-pass filter and intensity normalisation to adjust illumination levels across the laser sheet. Additionally, the initial calibration of the stereo PIV data is corrected using the built in Stereo-PIV self-calibration in Davis 10. Images were then processed with decreasing window sizes (64^2–16^2 px) and multipass-processed with 50 % overlap. Data were recorded with two cameras in parallel to increase spatial resolution of the field of view in the x–y plane, and resulting vector fields were stitched along the overlap using a weighted average. Data in the $x-y$ plane contain 10 000 image pairs, while in the stereo configuration in the $x-z$ plane, 3000 images were recorded. Each dataset was recorded as a single continuous recording. The chosen field of view results in a spatial resolution of 0.76 mm (0.03 in.) between vectors. The maximum seeding particle displacement in the accelerated free stream below the inverted wing ($U_\infty \approx 10\,\mathrm{m\,s^{-1}}$) was approximately 5 px. Illuminated particles were sufficiently large $\geqslant$1.5 px to avoid peak locking. Following the analysis of Adrian & Westerweel (2011), the uncertainty in the measured displacement

is approximately 0.1 pixel unit, which translates into a relative uncertainty of 2 % based on the free-stream velocity in the streamwise $x-y$ plane measurements. This is consistent with measurements in the x–z plane parallel to the wall. Statistical uncertainty is estimated following Wieneke (2017). The uncertainty of the mean is estimated as $U_{unc} = \sigma_u/\sqrt{N}$, where σ_u is the standard deviation of the streamwise velocity component and N the number of samples in the recording. The high recording frequency of time-resolved PIV can reduce the number of statistically independent samples. An estimate for the time between two independent samples is given by George, Beuther & Lumley (1978) as the integral time scale based on the auto-correlation coefficient ($\rho(t)$) of the respective time series ($T_{int} = \int_0^\infty \rho(t)\mathrm{d}t$). The effective number of independent samples is then derived from the overall time of the recording (T), relative to T_{int} following $N_{eff} = T/2T_{int}$. The result is a statistical uncertainty based on the effective number of independent samples, $\epsilon = \sigma_x/\sqrt{N_{eff}}$. For the planar PIV along the centreline, the maximum in T_{int} was found at ≈1.2 ms, resulting in an N_{eff} above 2000 samples in all cases. Use of the maximum integral time scale is considered in a conservative approach here. In a 95 % confidence interval the statistical error of the mean streamwise velocity u is $\epsilon_{u,95\,\%} \leq 1.5\,\%$ (analogue for v component is $\epsilon_{v,95\,\%} \leq 1.2\,\%$). The same method was applied to the wall-parallel planes with the same N_{eff}, resulting in $\epsilon_{u,95\,\%} \leq 1.2\,\%$ ($\epsilon_{v,95\,\%}$ and $\epsilon_{w,95\,\%} \leq 1\,\%$).

3. Post-processing methodology

3.1. *Spectral proper orthogonal decomposition*

The SPOD technique was used to find coherent spatiotemporal structures in the flow field. The SPOD in this work is based on the description in Towne, Schmidt & Colonius (2018). Similar to the algorithm of the traditional snapshot POD (solving a single eigenvalue problem for the covariance matrix, $\boldsymbol{C}$), the SPOD solves a series of POD problems in the frequency domain, one frequency at a time. The covariance matrix is therefore replaced by a cross-spectral density tensor.

The cross-spectral density tensor is constructed using Welch's method (Welch 1967) to determine cross-spectral densities for each time series. In the case of the PIV data, each velocity component at each PIV vector location is considered a single measurement. Consistent with Welch's method, the time series of N_t samples are segmented into a number N_k of blocks. The blocks are chosen to overlap increasing the number of realisations, and a window is applied along the temporal dimension of the data. A 50 % overlap was chosen with a Hamming window in this work.

On each block, the flow-field data are transferred into Fourier space using the discrete Fourier transform:

$$\hat{q}^{(k)}(f_m) = \sum_{j=0}^{N_{FFT}-1} q^{(k)}(t_{j+1}) e^{-i2\pi jm/N_{FFT}},\ k = -N_{FFT}/2+1, \ldots, N_{FFT}/2. \tag{3.1}$$

For each frequency, a data matrix is constructed combining data from the N_k blocks:

$$\hat{Q} = \left[\hat{q}^{(1)}\hat{q}^{(2)} \ldots \hat{q}^{(N_k)}\right], \tag{3.2}$$

where each $\hat{q}$ is a column vector with data from all spatial measurement locations (and velocity components) at the frequency of interest. The cross-spectral density for the

eigenvalue problem is found analogously to the POD:

$$\hat{\boldsymbol{C}} = \frac{1}{N_k - 1} \left\{ \hat{\boldsymbol{Q}}\, \hat{\boldsymbol{Q}}^H \right\}. \tag{3.3}$$

This leads to the following eigenvalue problem for each frequency:

$$\hat{C}\hat{\Phi} = \hat{\Phi}\hat{\Lambda}, \tag{3.4}$$

where $\hat{\Phi}$ are the eigenvectors and $\hat{\Lambda}$ contains the eigenvalues. Each eigenvalue problem is solved using the snapshot method typically used in the standard POD method (Sirovich 1987; Schmidt & Colonius 2020). The resulting eigenvalues are sorted in descending order. While eigenvalue spectra usually plot each mode as a separate solid line along all frequencies, neighbouring frequency bins are not necessarily describing similar flow features and are simply a representation of the most energetic feature at that respective frequency.

The data from PIV measurements provide velocity components on a regular grid as the input for q and as a result the sum of the eigenvalues represents twice the turbulent kinetic energy in the flow. In the following results, eigenvalues are scaled with the sum of all eigenvalues, representing the associated energy fraction.

3.2. *Bispectral mode decomposition*

Bispectral mode decomposition was developed to identify triadic nonlinear interactions from multidimensional data. A detailed representation of the method can be found in Schmidt (2020), and is briefly discussed here.

The fundamental idea is to detect quadratic phase coupling of triadic interactions by a measure of the bispectrum. For a stationary random signal, the bispectrum is defined as the double Fourier transform of the third moment (R_{qqq}), and provides a measure of the correlation of two frequencies with their sum:

$$S_{qqq}(f_1, f_2) = \int_{-\infty}^{\infty} \int_{-\infty}^{\infty} R_{qqq}(\tau_1, \tau_2) \mathrm{e}^{-i2\pi(f_1\tau_1 + f_2\tau_2)} \mathrm{d}\tau_1 \mathrm{d}\tau_2, \tag{3.5}$$

or in terms of the expectation operator (E):

$$S_{qqq}(f_1, f_2) = \lim_{T\to\infty} \frac{1}{T} E\left[\hat{q}(f_1)^* \hat{q}(f_2)^* \hat{q}(f_1 + f_2)\right], \tag{3.6}$$

where $\hat{q}(f)$ is the Fourier transform of the time-resolved signal ($q(t)$) and $(\,)^*$ the scalar complex conjugate. The algorithm used in this work (see Schmidt 2020) adapts Welch's method (Welch 1967) as an asymptotically consistent spectral estimator, to decrease the variance, by taking the ensemble average of the discrete Fourier transform over a number of overlapping blocks (N_N), assuming the input signal is statistically stationary.

Analogously to (3.6), an integral measure for the discrete point-wise bispectral density is defined as

$$b(f_k, f_l) = E\left[\int_\Omega \hat{q}_k^* \circ \hat{q}_l^* \circ \hat{q}_{k+l} \mathrm{d}x\right] = E\left[\hat{q}_{kol}^H W \hat{q}_{k+l}\right] = E\left[\langle \hat{q}_{kol} \hat{q}_{k+l} \rangle\right], \tag{3.7}$$

where $\hat{q}_{kol} = \hat{q}(x, f_k) \circ \hat{q}(x, f_l) = \hat{q}_k \circ \hat{q}_l$ is the entry-wise (Hadamard) product, where $\hat{q}_k = \hat{q}(x, f_k)$ denotes the kth frequency component, $(\,)^H$ the complex transpose, Ω the spatial domain of the flow and W a diagonal matrix of weights.

Next, the sum frequency component $\hat{q}_{k+l}$ and the product $\hat{q}_{kol}$ that form the resonant triad are defined by two linear expansions over the ensemble averages across the blockwise

realisations, using identical expansion coefficients a_i:

$$\Phi^{[i]}_{k\circ l} = \hat{Q}_{k\circ l} a_i, \tag{3.8}$$

$$\Phi^{[i]}_{k+l} = \hat{Q}_{k+l} a_i \tag{3.9}$$

for each (i) vector of expansion coefficients for the frequency doublet (k, l) and $\hat{Q}$ being the data matrix:

$$\hat{Q}_p = [\hat{q}^{(1)}_p \hat{q}^{(2)}_p \dots \hat{q}^{(N_k)}_p], \tag{3.10}$$

where p is either $k \circ l$ or $k + l$, respectively. The goal of the BMD is to optimally represent the flow field in terms of the bispectral density in (3.7). To ensure boundedness of the expansions in (3.8) and (3.9) the coefficient vector is chosen to follow the norm $||a_1|| = 1$, which leads to the maximisation problem:

$$a_1 = \underset{||a||=1}{\operatorname{argmax}} \left| E\left[\Phi^{[1]}_{k\circ l} W \Phi^{[1]}_{k+l}\right]\right| = \dots = \left| \frac{a^H E\left[\hat{Q}^{[1]}_{k\circ l} W \hat{Q}^{[1]}_{k+l}\right] a}{a^H a} \right|. \tag{3.11}$$

The right-hand side of the above equation is the Rayleigh quotient of the complex, non-Hermitian, square matrix ($B = E[\hat{Q}^{[1]}_{k\circ l} W \hat{Q}^{[1]}_{k+l}] \propto \hat{Q}^H_{k\circ l} W \hat{Q}_{k+l}$). The maximum of the Rayleigh coefficient is found by recasting the expression as an eigenvalue problem $(H(\Theta)a_1 = \lambda_1 a_1$, where $H = (1/2)(\mathrm{e}^{i\Theta} B + \mathrm{e}^{-i\Theta} B^H)$ and $0 \le \Theta < 2\pi)$, where the largest eigenvalue in the solution to this eigenvalue problem maximises (3.11) (Horn & Johnson 1994; Watson 1996). Here $\lambda_1(f_k, f_l)$ are referred to as the complex mode bispectrum. Furthermore the resulting expansion coefficients a_1 together with the data matrices in (3.8) and (3.9) lead to the bispectral modes Φ_{k+l} and the cross-frequency fields $\Phi_{k\circ l}$.

Additionally, interaction maps (Ψ) are defined based on (3.7) and (3.11), quantifying the local bicorrelation between the frequency triplet (f_k, f_l, f_{k+l}), showing regions of active triadic interaction:

$$\Psi = |\Phi_{k\circ l} \circ \Phi_{k+l}|. \tag{3.12}$$

4. Results

Results in this section are presented for the baseline case with the actuator installed and for several forcing amplitudes. Axis coordinates are given relative to the leading edge of the flat plate and are normalised with $L^*_\infty = 0.0254$ m (1 in.) according to the model design and corresponding to the same scaling chosen in the seminal work by Gaster (1967) and the experiments and numerical calculations in previous work using this model (Borgmann *et al.* 2025) discussing the baseline LSB without the actuator for the same free-stream conditions. The experimental conditions are identical to those reported in (Borgmann *et al.* 2020, 2021, 2022, 2025), at $Re_C = 90\,000$ based on the length of the inverted wing ($c = 8$ in. (20.3 cm)).

4.1. *Mean flow topology*

Time-averaged pressure coefficients ($C_p = p - p_\infty/0.5\rho U_\infty$) and select streamwise velocity contours are shown in figure 3. As expected, AFC reduces the size of the recirculation region. At the highest tested forcing amplitudes (7 kVpp) the pressure distribution is void of the characteristic C_p plateau and PIV does not detect reverse flow in the time-averaged velocity fields. However, the streamlines for the corresponding

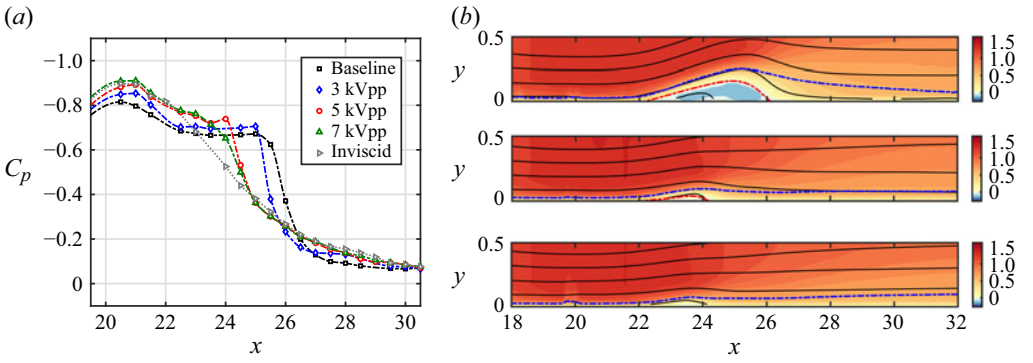

Figure 3. (*a*) Development of C_p for the baseline and several forced LSBs. (*b*) Velocity contours for the u component of the time-averaged flow field for the LSB for the baseline, $A_V = 5$ and 7 kVpp. Red dash-dotted line shows the boundary of the reverse flow; blue dash-dotted line is the displacement thickness (δ^*).

velocity field and the differences in the C_p distribution compared with the attached flow (quasi-'inviscid') suggest the existence of a shallow bubble in the time-averaged sense in this case. Following the experiments by Gaster (1967), the approximate or quasi-'inviscid' C_p distribution was measured for a tripped, turbulent boundary layer along the flat plate, which represents the case of a fully attached boundary layer. The development of the displacement thickness downstream of the LSB in figure 3 follows a downward trajectory in the baseline case, as a result of the changes in the local boundary layer from the significant displacement in the LSB to a turbulent boundary-layer profile downstream of reattachment. At moderate forcing amplitude (5 kVpp) the displacement thickness remains at a nearly constant height throughout the entire domain. At high forcing amplitudes (7 kVpp) changes in bubble topology are small; however, the displacement thickness follows an upward trajectory downstream of $x = 26$, expected for the downstream development of an attached boundary layer in the weak adverse pressure gradient downstream of the bubble.

The three-dimensional flow field in figure 4 was reconstructed from measurements in eight wall-parallel planes between $y = 0.08$ and $y = 0.39$. Results show a surface of constant streamwise velocity ($u/U_\infty = 0.8$, baseline; and $u/U_\infty = 0.87$, AFC) coloured with the standard deviation of the streamwise velocity fluctuations ($|u'|$). Data for the different wall-parallel planes are not synchronised in time and the reconstruction is limited to the time-average and statistical quantities. The baseline case appears largely 2-D with slight undulations across the span, related to only minor differences ($< 5\,\%U_\infty$) in the streamwise velocity in the time-averaged flow. The AFC at the two amplitudes in figure 4 causes significant spanwise variation of the streamwise velocity, indicated by the ridges in the contours of constant velocity in figure 4. For both AFC amplitudes these stationary spanwise undulations appear to be of some periodicity, but different wavelength. To estimate the spanwise wavelength in the wall-parallel plane, wavelength spectra are calculated for the $x-z$ plane closest to the maximum displacement thickness in each case. The dominant spanwise wavelengths of the time-averaged streamwise velocity ($|\overline{u}|$) are evaluated at each streamwise location (bottom row of figure 4). For the baseline, the dominant spanwise wavelengths in the shear layer of the LSB upstream of the maximum bubble height have a spanwise wavelength of $\lambda_{z,avg} \approx 1.6$. Downstream of reattachment, the dominant wavelength ($\lambda_{z,avg} \approx 0.75$) is only about half of those observed upstream. It should be noted that exact values for the spanwise wavelengths – in particular for large wavelengths – are difficult to obtain due to the small number of wavelengths within

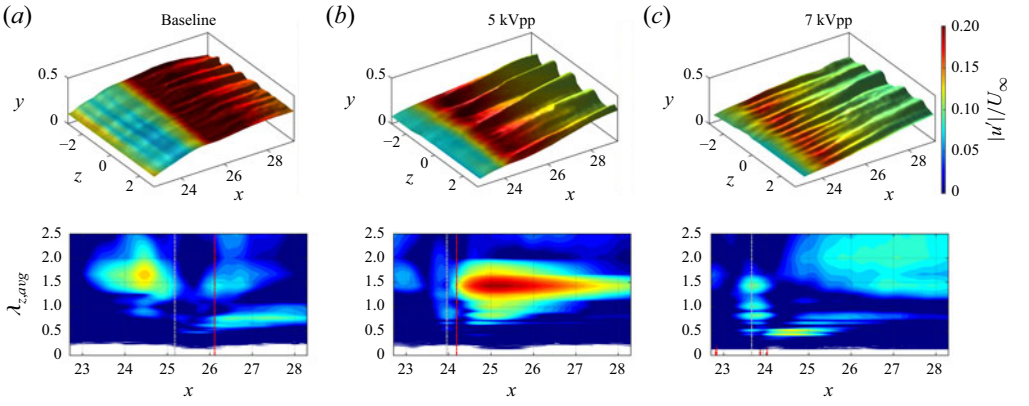

Figure 4. Time average of the reconstructed three-dimensional flow field. Shown is a plane of constant streamwise velocity ($u/U_\infty = 0.8$, baseline; and $u/U_\infty = 0.87$, AFC), coloured with the standard deviation of the local disturbances (u') for the (a) baseline and (b,c) forced LSBs. Grey and red vertical dash-dotted lines in the bottom panels are the location of maximum displacement thickness and reattachment, respectively. In the bottom panels, contours of the spanwise wavenumber extracted at each streamwise location in the flow field, in the measurement plane closest to δ^*_{max}.

the measurement domain and limited spatial resolution in $\lambda_{z,avg}$ (number of vectors along the spanwise domain). The large ridges observed in figure 4(b) downstream of the LSB at intermediate forcing amplitudes have an average wavelength of $\lambda_{z,avg} \approx 1.4$. Weak undulations near the maximum displacement thickness are in the range of $0.65 \leq \lambda_{z,avg} \leq 0.85$ at about half the wavelength of the dominant structures downstream. At high forcing amplitudes, the smaller spanwise structures in figure 4(c) have a spanwise wavelength of $\lambda_{z,avg} \approx 0.5$. Near the maximum bubble height, several wavelengths appear along a limited streamwise extent similar to the intermediate forcing amplitudes ($0.65 \leq \lambda_{z,avg} \leq 0.85$ and $\lambda_{z,avg} \approx 1.4$) and at $\lambda_{z,avg} \approx 0.5$ and ≈ 1. Downstream of reattachment at $x \approx 24$ the dominant spanwise wavelength is $\lambda_{z,avg} \approx 0.5$, consistent with the visual ridges in the range $24 < x < 26$ in the perspective view in figure 4(c). Other tested forcing amplitudes showed either very little spanwise periodicity in the time-averaged flow (< 5 kVpp, similar to the baseline) or a mix of the two presented cases (6 kVpp), suggesting that the differences in spanwise wavelength observed in the time-averaged flow depend on the forcing amplitude of the 2-D disturbances input upstream of laminar separation.

4.2. *Influence of forcing amplitude on the K–H instability*

Forcing of the dominant K–H instability in the shear layer via 2-D periodic excitation has been employed towards two different objectives in previous experimental work: (i) at low amplitudes as a diagnostic tool to allow tracking of the disturbance development in the shear layer without changing the LSB topology (Alam & Sandham 2000; Marxen *et al.* 2003; Diwan & Ramesh 2009; Kurelek *et al.* 2020) and (ii) at moderate amplitudes to investigate the flow response (Michelis *et al.* 2017; Yarusevych & Kotsonis 2017; Kurelek *et al.* 2018). The objective of the current work is to exploit the inherent disturbance growth due to the K–H instability, using relatively small disturbance input. The desired effect is the formation of strong 2-D vortical structures in the shear layer causing sufficient entrainment leading to reattachment of the boundary layer without the breakdown to turbulence, resulting in a delay of the transition that was previously only observed in numerical studies (Jones *et al.* 2008; Postl *et al.* 2011; Embacher & Fasel 2014; Benton &

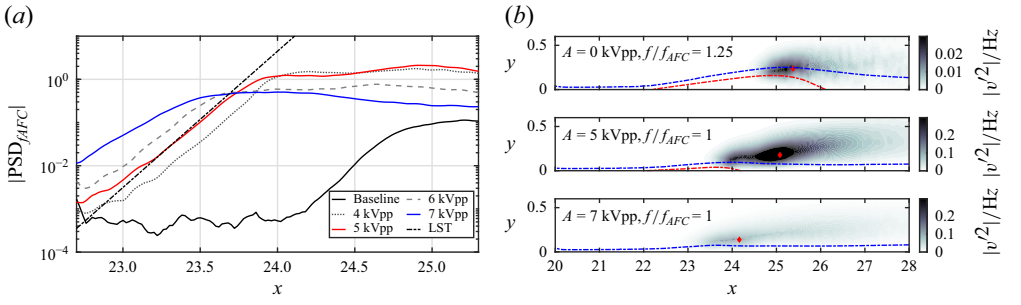

Figure 5. (*a*) Downstream development of the PSD amplitude of the v velocity component of the forced frequency ($f_{AFC} = 200$ Hz) and (*b*) PSD amplitudes of the v velocity component of the most amplified frequency (baseline, $f/f_{AFC} = 1.25$; AFC, $f/f_{AFC} = 1$), along the centreplane. Note the difference in the contour levels between the baseline (top) and forced cases (middle: 5 kVpp; and bottom: 7 kVpp). Red dash-dotted line: reverse flow boundary; blue dash-dotted line: δ^*; red marker: local amplitude maximum.

Visbal 2016; Gross *et al.* 2017). The results of Hosseinverdi & Fasel (2017) show that this type of flow control can be effective even in the presence of low levels of FST with transition observed in the boundary layer downstream of reattachment.

Active flow control raises the initial amplitudes of the forced frequency in the boundary layer upstream of separation. The location of the forcing was chosen near the onset of the adverse pressure gradient to mitigate the expected loss of disturbance amplitude in the preceding favourable pressure gradient and provide a wide range of amplitudes at laminar separation, to investigate the effect of the disturbance input to the transition process in the LSB or downstream of it. If the forcing frequency is within the band of most unstable frequencies for the LSB shear layer, the K–H instability is expected to 'lock on' to the forced frequency and cause exponential amplification of this periodic disturbance, and subsequent shedding of coherent vortical structures at the forced frequency. Forcing amplitudes in this work significantly modify the LSB downstream of the actuation (figures 3 and 4), possibly changing the stability characteristics of the resulting bubble. However, previous results in Borgmann *et al.* (2025) show that the LSB is most unstable to a broad band of frequencies (150 Hz $< f <$ 300 Hz), and numerical results suggest that the unstable characteristics of the shear layer do not significantly change for the forced bubble (Hosseinverdi & Fasel 2018), in particular upstream of amplitude saturation of the dominant 2-D mode.

Downstream development of the maximum disturbance amplitude of the $|v'|$ component in the boundary layer for the forced frequency is shown in figure 5(*a*). Results are based on $x-y$ plane measurements for the baseline $f_{AFC} = 250$ Hz ($f/f_{AFC} = 1.25$, with $f_{AFC} =$ 200 Hz) and several forcing amplitudes at $f_{AFC} = 200$ Hz ($f/f_{AFC} = 1$) as described in § 2.2. In all cases the development of the most dominant frequency is shown, which is different between the baseline (centre of the broad band) and the forced cases (locking on to the forcing frequency). Scaling the dimensional frequencies with the forcing frequency (f_{AFC}) highlights any direct relation of the data shown here to the fundamental mode or other harmonic content, in particular in the following sections. Growth of the initial disturbance amplitudes for forcing below 6 kVpp follows the linear trend (black dash-dotted line, figure 5*a*) predicted by LST for the most unstable frequency in the unforced LSB (Borgmann *et al.* 2025). At higher amplitude forcing, in particular at 7 kVpp, the disturbance growth is slowed down and notably saturates at significantly lower levels than for lower forcing amplitudes. The weaker amplitudes coincide with a smaller bubble and either a 'weaker' shear-layer mode or the earlier onset of nonlinear interactions at

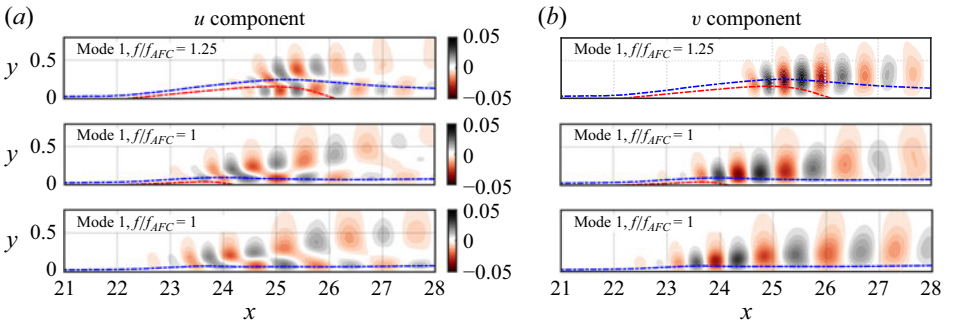

Figure 6. Real part of the SPOD modes (*a*) *u* and (*b*) *v* component for the K–H instability in the $x-y$ plane. Top to bottom: baseline, 5 and 7 kVpp; red and blue dash-dotted lines show the region of reverse flow and the displacement thickness, respectively.

such high forcing amplitudes. The global amplitude maximum for the forced frequency is observed at intermediate forcing amplitudes (4 and 5 kVpp). The maximum amplitude in these cases appears along a subtle 'secondary' peak downstream of the bubble and notably downstream of the initial amplitude saturation inside the LSB. Contours of the same $|v'|$ relative to the LSB in figure 5(*b*) locate the global disturbance amplitude maximum slightly downstream of the maximum bubble height for the unforced case (and for the highest forcing amplitude). For the intermediate forcing amplitude, two regions of significant amplitude are observed in the contours, corresponding to the initial saturation and the 'secondary' peak in the amplitude development (figure 5*a*), with the global disturbance amplitude maximum at a distance ($\Delta x \approx 0.8$) downstream of reattachment. The SPOD modes in figure 6 show the development of periodic structures in the shear layer for the same three cases. Highest amplitudes match the spectral analysis in figure 5(*b*), while indicating the existence of coherent structures far downstream of the LSB. Following the linear growth predicted by stability analysis, the onset of nonlinear interactions of the dominant 2-D mode (f_{AFC}) coincides with saturation of the dominant 2-D mode. Once nonlinear interactions occur, the 2-D mode is not expected to grow again.

The SPOD modes in the wall-parallel planes near the maximum displacement thickness (δ^*_{max}) in figure 7 show the three-dimensional development of coherent structures inside and downstream of the LSB related to the K–H instability. Coherent structures were observed following the initial exponential amplitude growth in the shear layer, in agreement with the amplitude development in figure 5(*a*). Unsurprisingly, the 2-D forcing significantly increases spanwise uniformity of the coherent structures in the LSB, and streamwise periodic structures remain at significant amplitudes throughout the entire measurement domain, even several bubble lengths ($L_{b,5\,\mathrm{kVpp}} = 2.1$) downstream of reattachment. The trajectory of the coherent structures follows the initial development of the displacement thickness (near the inflection point) downstream of separation and upstream of δ^*_{max}. Downstream of the LSB, the structures rapidly increase in size for all cases. In the wall-parallel planes, spanwise undulations of the initially 2-D structures are visible in the *u* component of the SPOD modes in figure 7(*a*). The spanwise wavelengths are consistent with those observed in the corresponding time-averaged flow fields (figure 4) and are likely related to the spanwise modulation of the mean streamwise velocity. Differences in the streamwise wavelength of the 2-D structures between the baseline and the forced cases are a direct result of the lower frequency of the forcing compared with the dominant frequency in the baseline case ($f/f_{AFC} = 1.25$). Both SPOD and amplitude development due to the K–H instability suggest that the largest amplitude

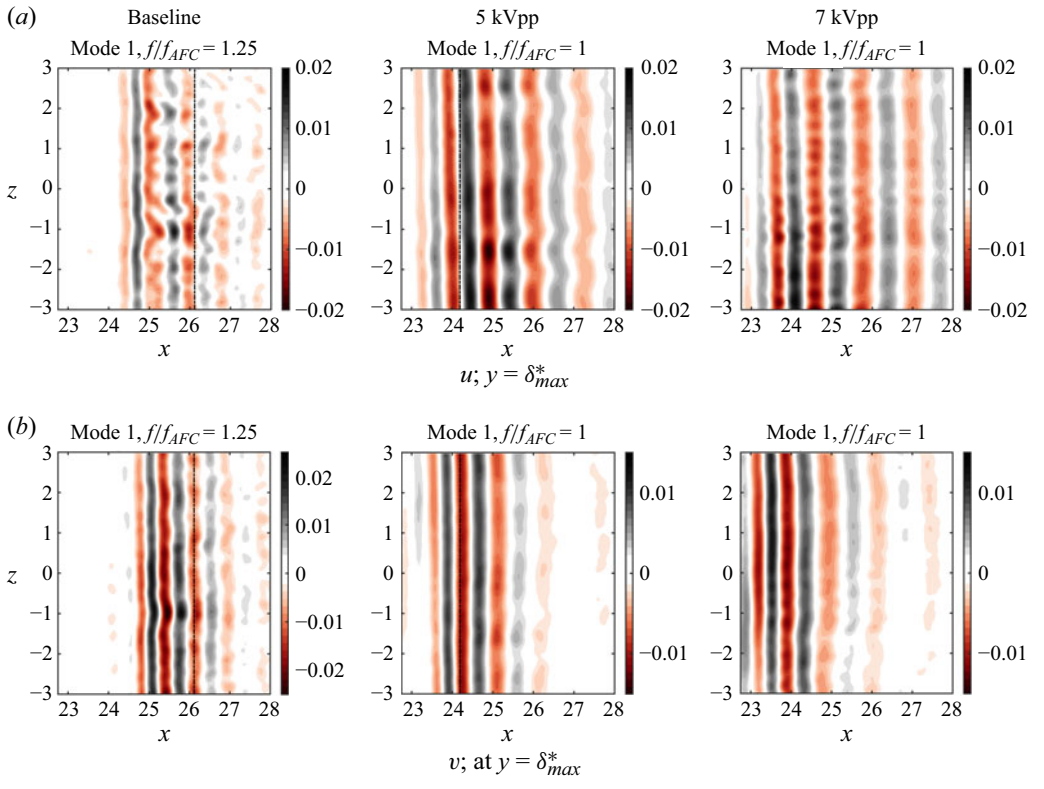

Figure 7. Real part of the SPOD modes (*a*) u and (*b*) v component for the K–H instability in the x–z plane at the location of the maximum displacement thickness $y = \delta^*_{max}$. Grey dash-dotted line shows the estimated reattachment location.

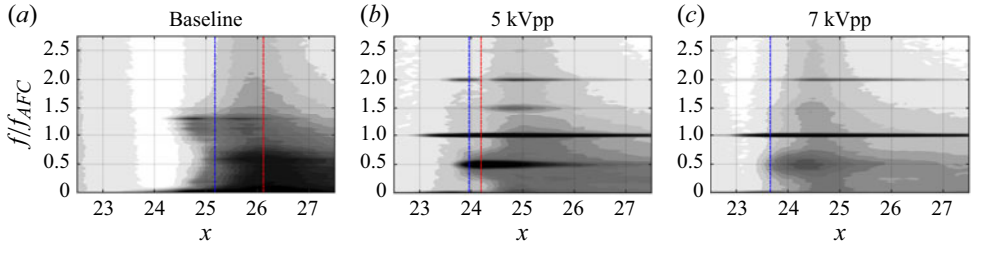

Figure 8. The PSD amplitude of u', spanwise-averaged in the x–z plane near the maximum displacement thickness δ^* for the (*a*) baseline and (*b*,*c*) several forcing amplitudes. Red and blue dash-dotted lines show the reattachment location and the location of maximum displacement thickness, respectively.

and 'best' spanwise uniformity of the dominant 2-D mode were achieved for intermediate forcing levels. A further increase in forcing amplitude limits the growth of the K–H mode in the shear layer and causes noticeably shorter spanwise 'ripples' (figure 7*a*, 7 kVpp) within the early stages of the 2-D structures.

4.3. *Unsteady characteristics downstream of linear disturbance growth*

The finite saturation in the K–H mode amplitude signals the onset of nonlinear interactions in the flow and eventual breakdown to turbulence. The differences in the spanwise wavelength in the mean flow (figure 4) and SPOD for the 2-D mode (figure 7) suggest

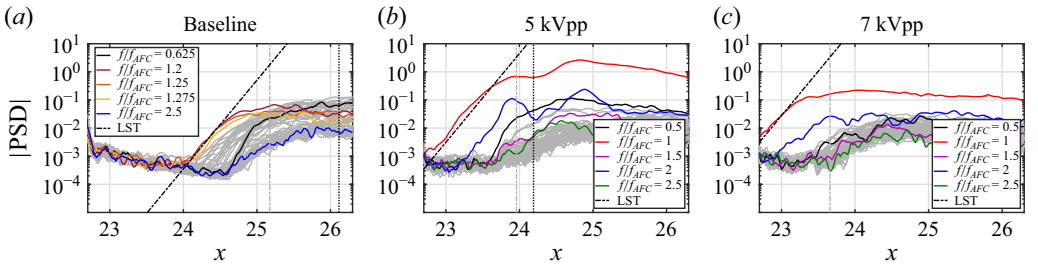

Figure 9. Maximum PSD amplitude in the boundary layer for the u' velocity component along the LSB. The LST for the unforced LSB is shown for reference (streamwise shifted to align with the observed growth in the respective case and shifted by an order of magnitude when compared with the AFC cases).

a change of the transition mechanism at different forcing amplitudes. Figure 8 shows contours of spanwise-averaged power spectral density (PSD) of the streamwise (u') fluctuations along the wall-parallel plane closest to the global maximum of displacement thickness in each case. The spanwise average was chosen to mitigate the effect of the three-dimensional base flow. In the baseline case, a lobe of most amplified frequencies ($0.75 < f/f_{AFC} < 1.5$) is observed upstream of the maximum bubble height ($24 \leq x \leq 25$) centred at a most unstable frequency of $f/f_{AFC} = 1.25$ in agreement with experiments and LST results from previous work on the unforced LSB (Borgmann *et al.* 2025). Just downstream of δ^*_{max}, significant spectral content in a broad range of frequencies around the subharmonic of the dominant 2-D mode ($f/f_{AFC} \approx 0.625$) and subsequently across the entire spectrum indicates the onset of transition in the LSB. Additional content at very low frequencies ($St < 0.1$) coincides with the typical frequency range of the large-scale, low-frequency motion of the reattachment location, often termed shear-layer 'flapping', similar to the reported values in the literature (e.g. Simoni, Ubaldi & Zunino 2014; Weiss *et al.* 2021; Malmir *et al.* 2024). With AFC, the PSD contours are dominated by the forced frequency. In both cases in figure 8, harmonic content is present starting just upstream of δ^*_{max}. In contrast to the baseline and high-forcing-amplitude cases, a significant narrow-band subharmonic is present for $A = 5$ kVpp. Further downstream, distinct narrow peaks appear at the half-harmonics $f/f_{AFC} = 1.5$ and, more subtly, at $f/f_{AFC} = 2.5$, where half-harmonics are half-integer harmonics of the fundamental frequency, $[n + 1/2]f_{AFC}$, for any integer n. While some broader content around the subharmonic is still observed at high forcing amplitudes, the broad band and lower amplitudes compared with the intermediate forcing case indicate a change in the transition mechanism. No half-harmonics are observed at high forcing amplitudes.

Comparison of the maximum amplitude development within the boundary layer in figure 9 agrees with the spanwise-averaged spectra in figure 8. Data are shown for the amplitudes of frequencies in the range $0 < f/f_{AFC} < 3$ for the u' velocity component (grey lines shown for each $\Delta f/f_{AFC} = 0.05$). Besides the initial linear growth of the K–H mode ($f/f_{AFC} = 1$ (1.25, baseline)), the amplitude development for the baseline case shows rapid growth of a subharmonic, at larger growth rates than the initial linear growth of the fundamental (K–H) mode, surpassing total amplitudes of the fundamental mode inside the LSB, between δ^*_{max} and the reattachment location. This location is associated with transition in the unforced LSB and coincides with the growth and saturation of a broad band of frequencies and the decay of the coherent structures in figure 6. Development of the maximum disturbance amplitude in the boundary layer for the forced cases in figure 9(*b*,*c*) confirms the initial linear growth of the fundamental, forced $|u'|$ disturbances, albeit over shorter streamwise distance for the higher forcing

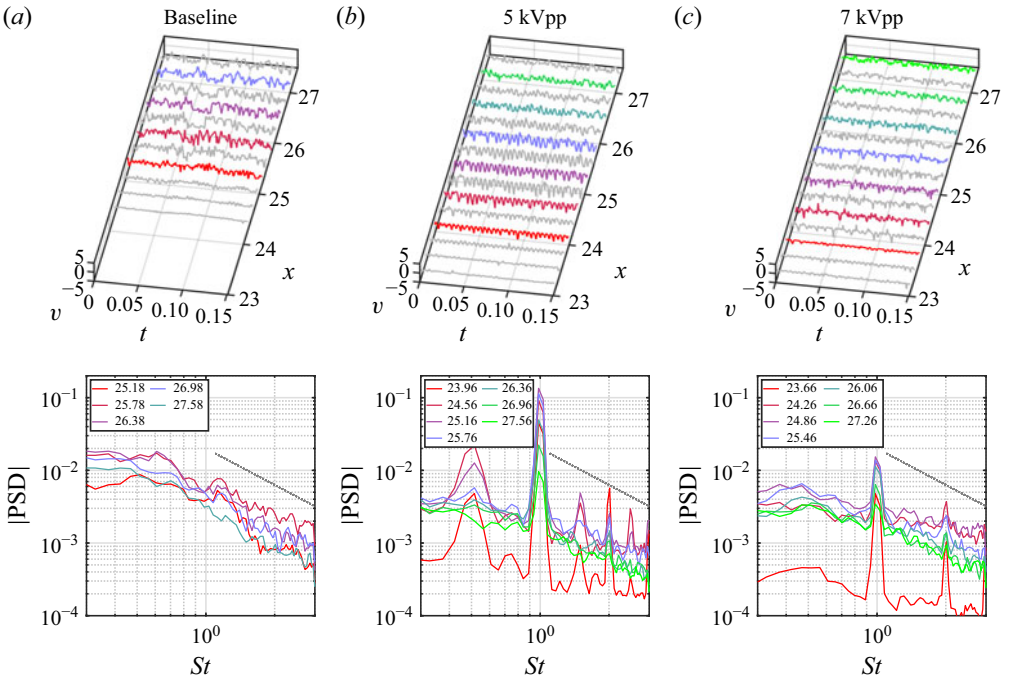

Figure 10. Sample from the time traces in the centreplane (x–y) for the (a) baseline and (b,c) several forcing amplitudes slightly above δ^* ($\delta^* + 0.06$). Red: time trace at the location of maximum displacement thickness.

amplitude. Saturation of the fundamental mode is observed near δ^*_{max}, with significantly higher amplitudes for the intermediate forcing amplitudes compared with the baseline and high-amplitude forcing. Growth of a harmonic is consistently observed alongside the fundamental mode for both forcing cases analogous to the numerical simulations by Embacher & Fasel (2014). At intermediate forcing amplitudes, the subharmonic ($f/f_{AFC} = 0.5$) experiences strong initial growth just upstream of δ^*_{max}. The subharmonic reaches its maximum at $x = 24.6$ downstream of the LSB, but never exceeding the amplitudes of the fundamental mode. The amplitudes of the subharmonic (and harmonic) as well as the half-harmonics at $f/f_{AFC} = 1.5$ and to a lesser degree at $f/f_{AFC} = 2.5$ precede the broad-band amplitude growth and saturation in the spectra in the intermediate forcing case (figure 9b). The only frequencies with amplitudes above those of the half-harmonics are near the subharmonic. The results suggest that for a limited streamwise distance (between the upstream shear layer and just downstream of reattachment) only a few modes, related to the harmonics, sub- and half-harmonics, are of relevant amplitude. The later onset of broad-band amplitude growth towards and downstream of the estimated reattachment location of the time-averaged LSB suggests a delay of the transition to a location downstream of the LSB. This is in contrast to the behaviour at high forcing amplitudes, which shows no spectral content related to the half-harmonics and onset of a broad-band amplitude growth near δ^*_{max} (at 7 kVpp) alongside and earlier saturation (24.3).

Time traces of the streamwise velocity inside the shear layer just above the local displacement thickness ($\delta^* + 0.06$) at several streamwise locations are shown in figure 10 alongside corresponding power spectra. Data are evaluated slightly further away from the wall to avoid discontinuities in the PIV time traces near the wall without relying on

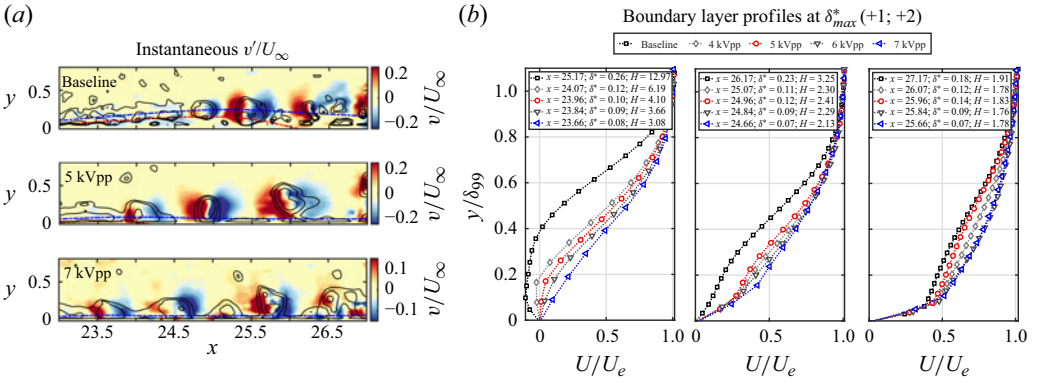

Figure 11. (*a*) Instantaneous snapshots of the baseline and forced flow field and (*b*) boundary-layer profiles.

interpolation. For the baseline, only weak periodicity is present upstream of δ^*_{max}. Rapid growth of broad-band disturbances quickly leads to a loss of periodicity and a chaotic or rather transitional signature in the subsequent time traces and PSDs, approaching the $-5/3$ slope prior to the time-averaged reattachment location. In the forced cases, periodic disturbance input leads to a near-sinusoidal signal upstream of δ^*_{max}. While the velocity fluctuations retain strong periodicity at intermediate forcing amplitude, until $x \approx 26$, further increase of the forcing amplitude causes time traces to appear rather chaotic and comparable with those of the early transition observed in the baseline case, albeit at lower amplitudes. Corresponding power spectra retain a significant amplitude for the fundamental mode throughout the domain when flow control is applied. Spectra for the intermediate forcing cases again show the subharmonic and half-harmonics upstream of the breakdown of periodicity in the time traces ($x = 26$). Spectra for both AFC cases approach the $-5/3$ slope for $x > 26$, while still containing a peak around the forced frequency, which at intermediate forcing amplitudes remains an order of magnitude above other spectral content up to $x = 27.5$.

Besides the moderate- and high-frequency content in the LSB shear layer, significant spectral content was observed at very low Strouhal numbers typically associated with shear-layer 'flapping' $St = f L_b/U_\infty < 0.1$ ($f/f_{AFC} < 0.075$, for $L_{b,5\,\mathrm{kVpp}}$) in the baseline case and at marginal (3 kVpp) forcing amplitudes (not shown). Based on the spectral analysis in figures 8 and 10, AFC amplitudes $\geqslant 4$ kVpp stabilise the shear layer and do not show any significant low-frequency content (no 'flapping').

Instantaneous velocity fields (v) in figure 11(*a*) are overlaid with Γ_2 vortex contours to show the location of clockwise-rotating vortex structures. The Γ_2 contours are based on a non-local, Galilean-invariant scheme using integration to identify the strength and rotation of vortical structures in the flow (Graftieaux, Michard & Grosjean 2001). It is therefore especially suited for 2-D experimental data, avoiding the numerical differentiation involved with other more common criteria. Originating in the shear layer of the LSB, the pairs of red and blue contour levels indicate the periodic wall-normal disturbance waves growing along the shear layer and propagating downstream as clockwise-rotating vortices. Two vortical structures can be observed in the baseline case near the downstream portion of the bubble, and following the previously discussed transition inside the bubble. Breakdown of the coherent structures appears around reattachment for the representative cases shown here. With AFC, several coherent structures are observed downstream of the LSB. Most notably a 'clean' vortex is identified at $x = 25$ downstream of reattachment at intermediate forcing amplitudes, before the structures appear distorted further downstream ($x > 26$).

This is in agreement with the loss of periodicity observed in the time traces (figure 10) and the decrease in amplitude of the K–H mode (figures 5*a* and 9). Unsurprisingly, the higher forcing amplitudes do not further increase the coherence in the flow field. Superposition of the strong clockwise-rotating vortices resulting from the K–H instability in the LSB shear layer with the mean flow causes a modification of the local time-averaged velocity profiles. The result is an increase in the streamwise velocity at the edge of the boundary layer (δ_{99}; see figure 3) and a velocity deficit inside the boundary layer. Comparisons of time-averaged boundary-layer profiles are shown in figure 11(*b*) for several streamwise locations at and downstream of the respective location of δ^*_{max} (maximum bubble height). Inside the LSBs, the boundary-layer profiles show the successive decrease in bubble size with an increase in forcing amplitude. Downstream of reattachment ($> \delta^*_{max} + 1$), several of the forced cases show a notable velocity deficit in the local boundary layer. Forcing at intermediate amplitudes (5 kVpp) creates the largest such deficit in the boundary-layer profiles, suggesting the presence of strongest vortical structures in this case, even downstream of the LSB. The larger deficit in the baseline is a result of the significantly larger separated region and relative proximity of $\delta^*_{max} + 1$ to the mean reattachment location. However, at the most downstream locations shown in figure 11(*b*) the remaining velocity deficit in the boundary layer for the intermediate case is near that of the baseline case and significantly differs from the approximately turbulent boundary-layer profile observed at high forcing amplitudes. The delayed breakdown of vortical structures and associated velocity deficit further supports the observed delay in the turbulent breakdown, in particular at intermediate forcing amplitudes.

The observation of delayed growth of broad-band disturbances in figure 9(*b*), the strong periodicity in the time traces in figure 10(*b*) and the presence of strong vortical structures downstream of reattachment (figure 11) suggest that at least at the intermediate forcing amplitude, the transition process is delayed, causing the dominance of a single mode in the shear layer and downstream of reattachment, followed by only its subharmonic and harmonic leading to observable interactions in the form of half-harmonics in the power spectra in figure 8. However, further increase in forcing amplitude does not increase this effect and appears to cause early onset of transition in the LSB in comparison. This suggests that, in contrast to separation control, the optimal forcing amplitude for transition delay is found at moderate amplitudes and coincides with the case for the global maximum in the K–H mode amplitude (figure 5*a*), similar to the numerical results in Embacher & Fasel (2014) and Hosseinverdi & Fasel (2018, 2019). To the authors' best knowledge, this is the first experimental evidence for simultaneous transition delay and separation control in LSBs (previously observed only in numerical simulations in Embacher & Fasel (2014) and Hosseinverdi & Fasel (2018)). Other such examples, also by the authors, were shown only for airfoils, similar to, for example, Benton & Visbal (2018), but were inconclusive due to the very thin boundary layers in those experiments (Agate *et al.* 2018).

4.4. *Relevant triadic interactions in the forced LSB*

Linear growth of the 2-D mode downstream of laminar separation follows the predicted growth rates from linear stability calculations for all but the highest tested amplitudes. Additionally, in all cases, the dominant K–H mode reaches finite amplitudes inside the LSBs and is followed by the interaction of this dominant 2-D mode with other disturbances at various frequencies, eventually leading to transition. Growth of both subharmonic and fundamental (harmonic) modes was observed following the saturation of the K–H instability in previous work (Maucher *et al.* 2000; Jones *et al.* 2008; Marxen *et al.* 2013). Results for the baseline case in this work, i.e. figure 9, suggest that the transition in the

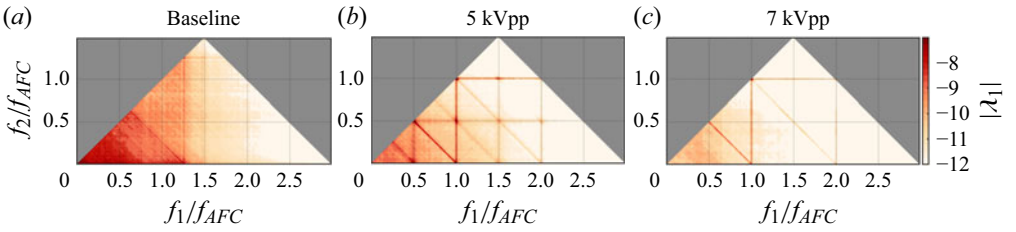

Figure 12. The BMD spectra in the centreplane (x–y) for several forcing amplitudes.

unforced LSB is a result of the growth of a subharmonic mode, exceeding maximum amplitudes of the 2-D mode prior to reattachment (figure 9). While this subharmonic is observed at significant amplitudes up to the intermediate forcing case, with maximum amplitudes downstream of reattachment, its maximum amplitudes are found to decrease towards the highest tested forcing cases.

The BMD technique was introduced by Schmidt (2020) to identify nonlinear interactions in time-resolved flow-field data. Bispectra of the velocity signal at each spatial location in the measurement domain identify coherent structures and provide information about the strength and location of triadic interactions in the flow. These triadic interactions connect two frequency components (f_1 and f_2) to their sum-frequency (f_3). The method combines the spatiotemporal analysis of the SPOD with cross-bispectral analysis to represent the second-order statistics in the data, providing a measure of quadratic nonlinear interaction of any pairwise combination of frequencies in the flow (see § 3).

The BMD spectra are shown in figure 12 for the baseline and the cases of intermediate and high forcing amplitude. In figure 12, the horizontal and vertical axes are for the non-dimensionalised frequencies f_1/f_{AFC} and f_2/f_{AFC}, respectively. The third component in each triadic interaction is the sum of frequencies $f_1 + f_2 = f_3$. The colour contours identify the strength of the respective interactions. Similar to the power spectra in figure 8 the baseline case is dominated by low-frequency content, showing only weak interactions of a broad band of low frequencies. It should be noted here that the lines in the BMD spectra are a by-product of spectral leakage and appear in all cases of significantly lower amplitudes than the connecting peaks, and are not considered in the following analysis (Schmidt 2020). Elevated contour levels are observed near the dominant frequency in the unforced flow ($f_1/f_{AFC} = 1.25$ and $f_2/f_{AFC} = 0$) and below its subharmonic ($f_1/f_{AFC} = f_2/f_{AFC} = 0.625$). Slightly elevated content in the BMD spectra is present around the fundamental mode, for $f_1/f_{AFC} = f_2/f_{AFC} = 1.25$ (where $f_3/f_{AFC} = (f_1 + f_2)/f_{AFC} = 2.5$). This interaction is termed the sum self-interaction since $f_1 = f_2$, in this triad. The interaction of $f_1/f_{AFC} = 1.25$ with $f_2/f_{AFC} = 0$ ($f_3/f_{AFC} = 1.25$) is characteristic of a difference self-interaction with $f_1/f_{AFC} = -f_3/f_{AFC}$ (Schmidt 2020). An example for difference self-interaction is the interaction of two oblique waves propagating in opposite directions at the same frequency, potentially leading to stationary ($f = 0$) structures. Such interactions are of particular interest in this work, with respect to the large spanwise modulation of the mean flow in figure 4. In the following, the frequency triplets for the triadic interaction will use the short notation $[f_1;\ f_2;\ f_3]/f_{AFC}$, i.e. [1.25; 1.25; 2.5] for the previous example. The difference self-interaction for $f_1/f_{AFC} = -f_3/f_{AFC}$ (Schmidt 2020) will follow the notation consistent with its location in the BMD spectra, which is located at [1.25; 0; 1.25].

At intermediate forcing amplitudes, several triadic interactions are of significant amplitude in the BMD spectrum. Most notable peaks in the spectra are at the difference self-interaction of the subharmonic and fundamental mode, and their sum self-interactions

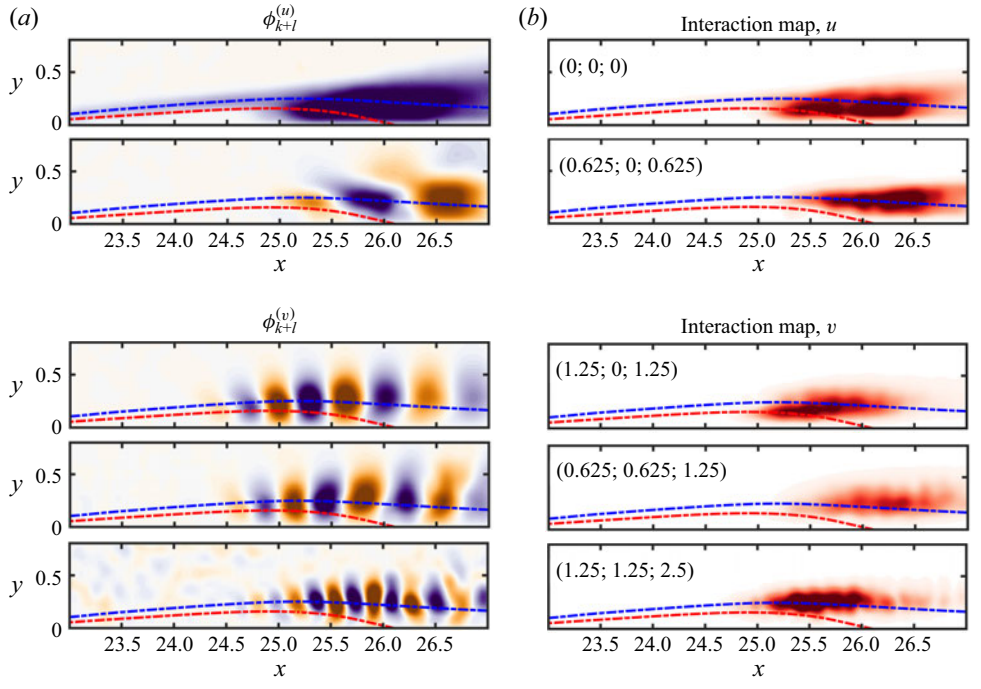

Figure 13. Dominant BMD mode interactions for the baseline case, select mode u' and v' components. Contour levels are normalised by the respective maximum ($|u'|$ or $|v'|$) in each case; for relative mode amplitudes, see figure 12.

([0.5; 0; 0.5], [1; 0; 1], [0.5; 0.5; 1] and [1; 1; 2]). Furthermore, interaction of the fundamental mode with the subharmonic ([1; 0.5; 1.5]) and, albeit weaker, interaction of the fundamental with an additional higher half-harmonics at $f/f_{AFC} = 2.5$ ([1.5; 1; 2.5]) seem relevant. The interaction of the subharmonic and fundamental mode readily explains the half-harmonic, as previously discussed in the spectral analysis in figure 10. Subsequent interaction of either this half-harmonic with the fundamental or the first harmonic and subharmonic can lead to the half-harmonic at $f/f_{AFC} = 2.5$ through either [1.5; 1; 2.5] or [2; 0.5; 2.5]. At high forcing amplitudes, the number of notable triadic interactions is reduced to the self-interactions of the fundamental (sum and difference), the difference self-interaction of the first harmonic ([2; 0; 2]) and a weak self-interaction of the subharmonic ([0.5; 0.5; 1]). The dominant peaks in the BMD spectra confirm the highest amplitudes observed in the PSDs in figure 8 and the key frequencies in the amplitude development plots in figure 9.

In addition to the identification of dominant nonlinear (triadic) interactions in the flow, the BMD eigenfunctions provide spatial information about the mode shape of the relevant interactions and an interaction map, visualising regions of active triadic interaction in the flow. The eigenfunctions of the sum-frequency component $\hat{q}_{k+l}$ appear nearly identical to the mode 1 eigenfunctions from the SPOD for the frequency of f_3 (Schmidt 2020) and show the spatial coherent structures related to the sum-frequency component.

Notable triadic interactions for the baseline case in the $x-y$ plane are shown in figure 13. The difference self-interaction of the 'zero' frequency reflects quasi-stationary structures as well as low-frequency behaviour ($St < 0.01$, [0; 0; 0]) due to the frequency binning in the Fourier transform (via fast Fourier transform) used in the BMD. The baseline LSB experiences so-called shear-layer 'flapping' causing a subtle movement of the initial

shear layer and separation location, alongside a large-scale motion of the reattachment location, most obvious in the streamwise component of the BMD mode in figure 13(*a*) (Spalart & Strelets 2000; Hain, Kähler & Radespiel 2009; Michelis *et al.* 2017; Istvan & Yarusevych 2018; Singh 2019). The BMD modes in figure 13 (left column) and subsequent plots are shown for the sum-frequency component, showing coherent structures related to the frequency content f_3. The BMD modes are qualitatively similar to the SPOD modes (mode 1) for the same frequency.

Interaction maps show the onset of nonlinear behaviour in the difference self-interaction of the fundamental mode ([1.25; 0; 1.25]) below the location of the local displacement thickness, closer to the region of reverse flow inside the LSB. The streamwise location of this interaction coincides with the saturation of disturbance amplitudes (following its linear growth) in figure 9 and the growth of the harmonic ([1.25; 1.25; 2.5], along the shear layer). The triadic interaction [0.625; 0.625; 1.25] relates the subharmonic to the fundamental mode, with the onset of the interaction downstream of the sum-frequency component (interaction map in figure 13*b*, relative to BMD mode in figure 13*a*). Existence of a relevant triadic interaction between the fundamental mode and subharmonic suggests some form of subharmonic resonance in the separated shear layer (Ho & Huerre 1984; Husain & Hussain 1995). Onset of all interactions shown in figure 13 lies within the LSB between the location of maximum bubble height and reattachment. This is also true for all other triadic interactions, not shown here, indicative of the rapid transition inside the unforced LSB (Hosseinverdi & Fasel 2019).

In the presence of AFC, the fundamental mode is significantly amplified. The BMD eigenfunctions and interaction maps in figure 14 are plotted for only one velocity component for each case, chosen to best represent the interaction. Strong nonlinear self-interaction of the fundamental mode near reattachment leads to a strong harmonic mode, at intermediate forcing amplitudes (figure 14). The interaction map for the [0.5; 0.5; 1] mode shows high amplitudes downstream of reattachment. However, the fundamental mode ($f_3/f_{AFC} = 1$ in figure 14*a*) upstream of the interaction suggests that strong amplification of the subharmonic is a result of the fundamental mode. The onset of the [0.5; 0.5; 1] mode interaction appears alongside the interaction of the subharmonic with the fundamental ([1; 0.5; 1.5]) and the sum self-interaction of the fundamental mode ([1; 1; 2]). Slightly downstream, the onset of the difference self-interactions of the subharmonic and fundamental, respectively, are observed ([0.5; 0; 0.5], [1; 0; 1]). Contrary to the baseline, no significant nonlinear interactions are found at the low frequencies related to the 'flapping' motion of the shear layer. Furthermore, the self-interaction of the low-frequency mode and the example shown in the bottom row in figure 14 for a 'random' pair of frequencies is negligible upstream of $x = 25.5$ and only gains significant strength further downstream (this is true for all interactions except for the relevant ones shown in the top five rows of figure 14). This provides further evidence to the later onset of broad-band nonlinear interactions and amplitude growth, corroborating the delay of transition downstream of the LSB in this case.

At higher forcing amplitudes, the sum self-interaction of the fundamental is most dominant (figure 15). Bispectral modes, cross-frequency fields and interaction maps for this interaction show the presence of the resulting harmonic throughout the domain, with significant triadic interaction along the LSB in this case. The early onset of this mode suggests the early onset of these nonlinear interactions, possibly in the boundary layer upstream of the LSB and could explain the weaker finite amplitudes and slightly reduced linear growth rates of the fundamental mode (figure 5*a*). Other significant triadic interactions related to the fundamental mode in figure 15 appear simultaneously, with the onset of the interactions just downstream of the maximum displacement thickness (δ^*_{max})

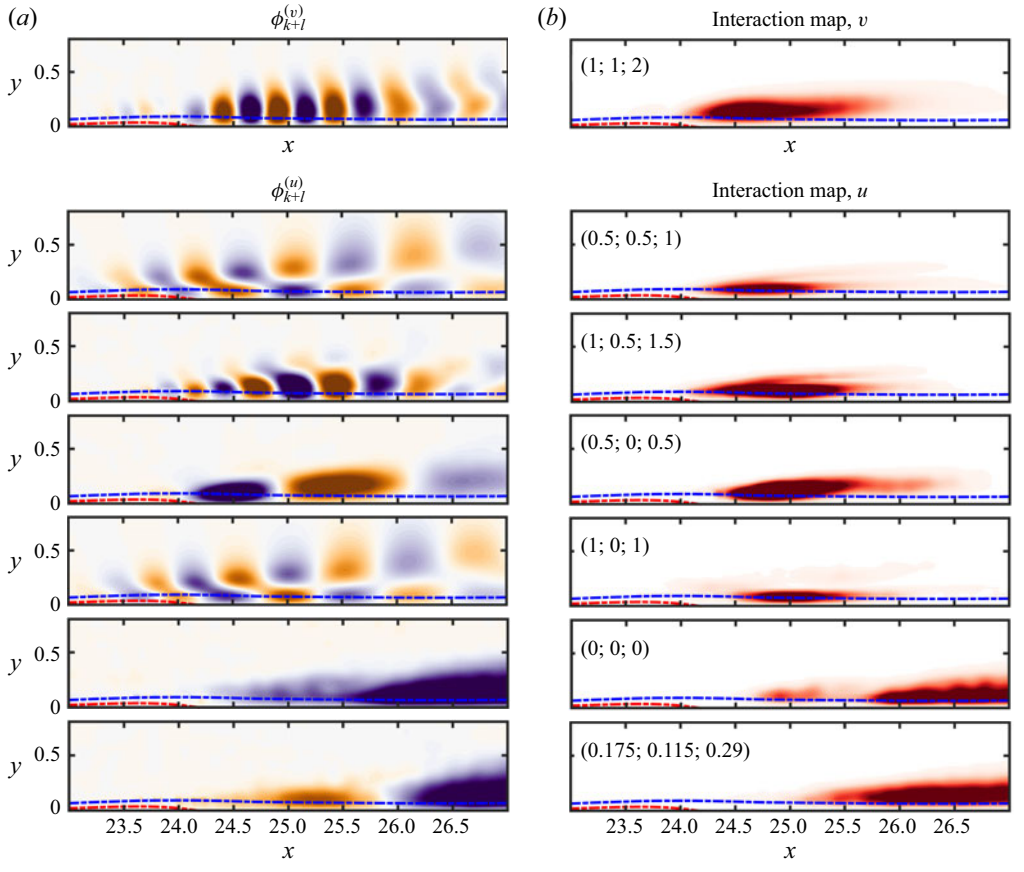

Figure 14. Dominant BMD mode interactions for the intermediate forcing case (5 kVpp), order based on location of streamwise maximum. Contour levels are normalised by the respective maximum ($|u'|$ or $|v'|$) in each case; for relative mode amplitudes, see figure 12.

and maxima in the range $24.5 < x < 25$. Of particular interest are again the last two rows in figures 14 and 15, showing the low-frequency mode and an example of a 'random' interaction in the flow. The streamwise location of the onset of broad-band nonlinear interactions at high forcing amplitudes coincides with the onset of the triadic interaction of the dominant modes found in the BMD spectra (except the sum self interaction of the fundamental mode, [1; 1; 2]). This is in contrast to the intermediate forcing case with interactions – other than the dominant modes in the BMD spectrum – notably delayed downstream, consistent with the observations of the later breakdown in the time traces (figure 10).

The dominant mode in the LSB shear layer (baseline and AFC) is expected to be largely 2-D (figure 7). However, large three-dimensional structures in the mean flow in figure 4 suggest strong periodic spanwise modulation of the LSB. To compare the spanwise wavelength of the nonlinear modes with the spanwise periodic structures in the unsteady mean flow, BMD is applied to the wall-parallel measurements. The BMD spectra in the $x-z$ planes are very similar to those observed for the $x-y$ plane measurements (figure 12) and therefore not repeated here for brevity.

In the baseline case, weak three-dimensionality is present only in the BMD eigenfunctions and interaction maps for the low-frequency ('zero') mode and in the

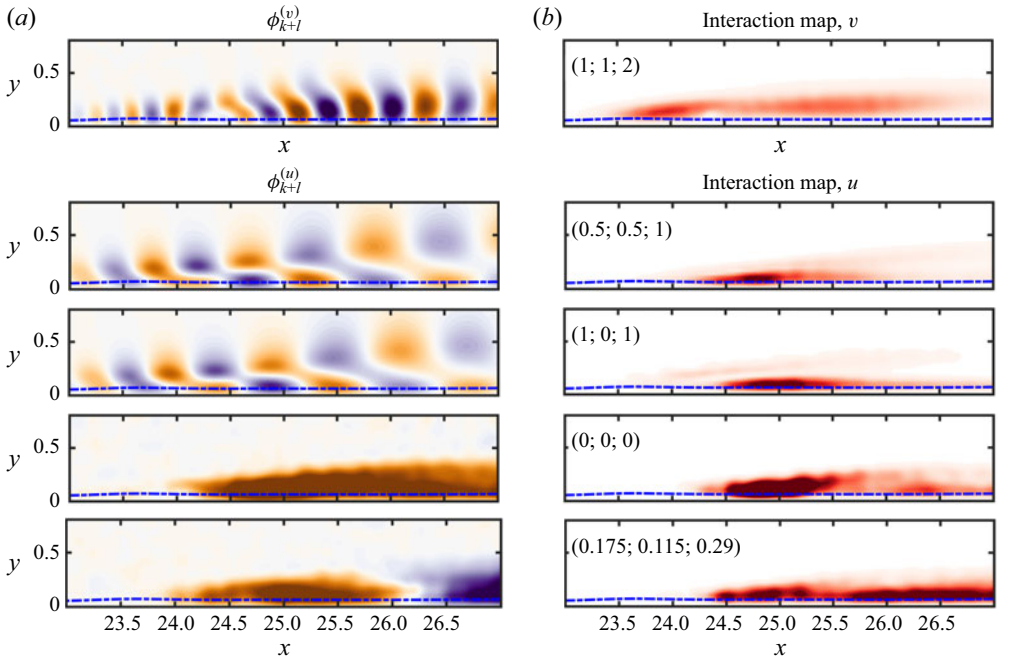

Figure 15. Dominant BMD mode interactions for the intermediate forcing case (7 kVpp), order based on location of streamwise maximum. Contour levels are normalised by the respective maximum ($|u'|$ or $|v'|$) in each case; for relative mode amplitudes, see figure 12.

difference self-interaction of the fundamental mode and subharmonic (figure 16). Streamwise streaks in the BMD eigenmodes appear around the maximum displacement thickness in the bubble and agree in spanwise wavelength with the weak stationary structures in figure 4(*a*). The spanwise uniform structure in the [0; 0; 0] mode in the range $23.5 < x < 24$ coincides with the inflection point in the upstream shear layer and is void of spanwise modulation and nearly 2-D (differences in the streamwise location are a result of a slight tilt in the measurement plane across the span). The interaction maps of the difference self-interaction of the fundamental mode and subharmonic show similar streaks beginning at the same streamwise location. The similarity in the dominant spanwise wavelength ($\lambda_z \approx 0.75$) to previous global stability analysis (Borgmann *et al.* 2025) and the quasi-stationary character of the streamwise streaks in the 'zero'-mode interaction (and the time average, figure 4*a*) suggest that these could be the result of a global instability in the unforced LSB. The BMD (and SPOD) eigenmode for the subharmonic (figure 16*b*) shows a deformation of spanwise-coherent structures at a wavelength of $\lambda_z \approx 1.5$, twice that of the mean flow deformation. This modulation of the 2-D structures in the shear layer leads to $\lambda_z/\lambda_x \approx 2$, and is well within the range of wavelength ratios reported for the spanwise modulations in Rodríguez *et al.* (2021), who report spanwise deformation of the entire separated region as a result of the saturation of the primary 2-D instability. Both of these wavelengths are observed in the time-averaged flow (figure 4*a*) and are related to stationary structures or at least very low frequency.

With AFC, the fundamental mode was significantly strengthened. Figure 17 shows the difference and sum self-interactions of the fundamental mode for the forced flow (5 and 7 kVpp). The BMD eigenmodes for [1; 0; 1] show the spanwise-coherent structures expected from figure 6. Differences can be seen in the spanwise modulation of the K–H

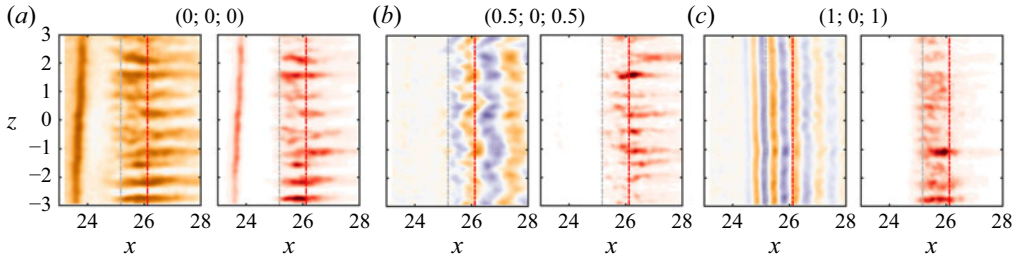

Figure 16. The BMD modes; $\Phi_{k+l}^{[u]}$ and interaction maps of the u velocity component for the baseline. Contour levels are normalised by the respective maximum ($|u'|$ or $|v'|$) in each case; for relative mode amplitudes, see figure 12.

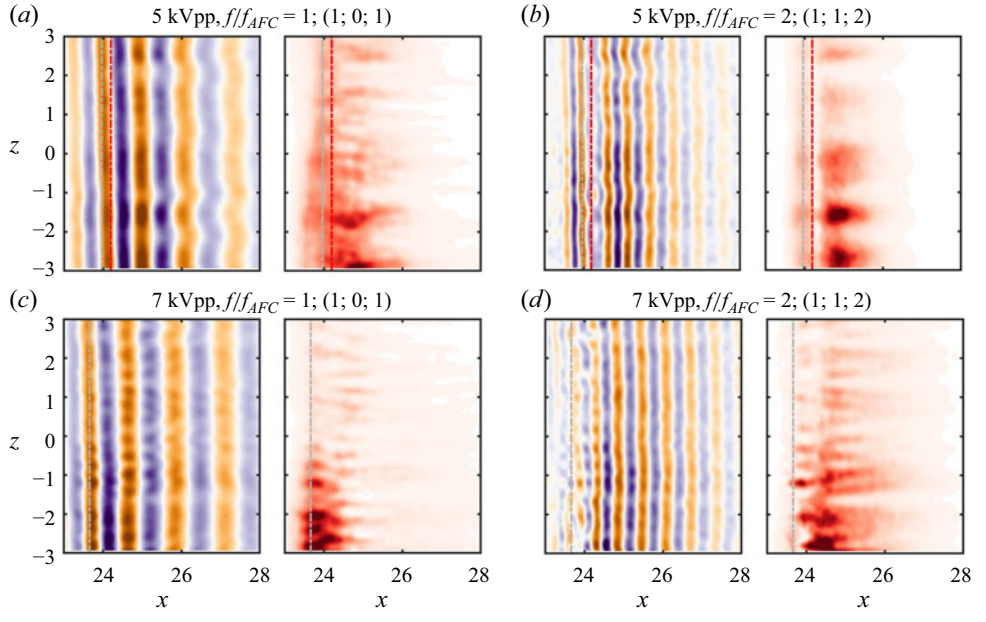

Figure 17. The BMD modes related to the subharmonic and corresponding interaction maps for the forced LSB: (*a*,*b*) 5 kVpp; (*c*,*d*) 7 kVpp. Contour levels are normalised by the respective maximum ($|u'|$ or $|v'|$) in each case; for relative mode amplitudes, see figure 12.

mode for different forcing amplitudes. Both interaction maps ([1; 0; 1] and [1; 1; 2]) at moderate forcing amplitudes are dominated by large-scale spanwise undulations. The mode shape of the sum self-interaction of the fundamental mode agrees with the streamwise wavelength of the harmonic mode in SPOD. Largest amplitudes in the interaction maps for the harmonic are located downstream of reattachment ($x = 25$) with a spanwise organisation identical to that of the large-scale stationary undulations in the mean flow in figure 4(*b*) ($\lambda_z \approx 1.4$). At the high forcing amplitude, the interaction maps in figure 17 seem dominated by smaller-scale spanwise modulations, present in the sum-frequency components (mode shapes) of both the fundamental and harmonic and their interaction maps. The small-scale structures experience a phase shift near $x = 24$ for [1; 0; 1] resulting in a staggered pattern near the bottom of figure 17(*c*) (the differences along the spanwise direction are likely a result of strong local gradients and the slight tilt of the measurement plane). Similar behaviour, albeit weaker, is observed further downstream

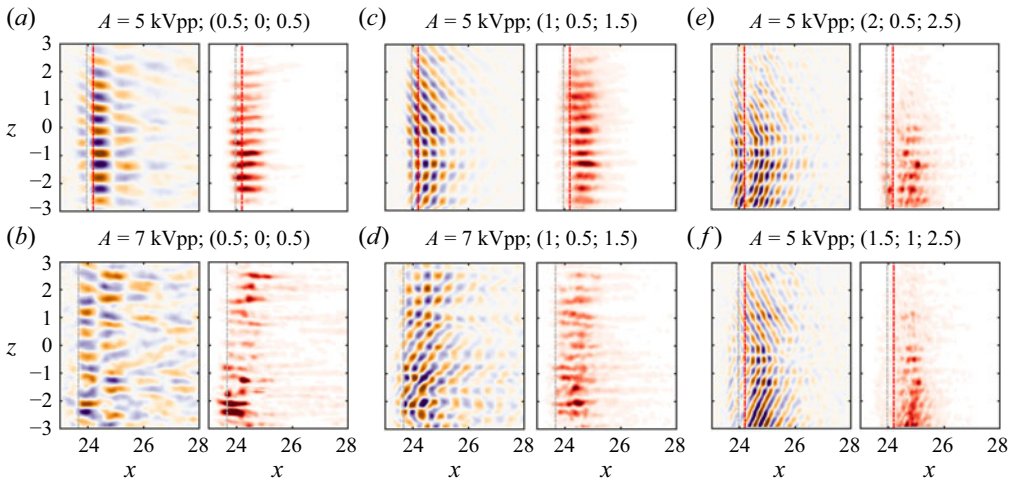

Figure 18. The BMD modes related to the subharmonic and corresponding interaction maps for the forced LSB. Contour levels are normalised by the respective maximum ($|u'|$ or $|v'|$) in each case; for relative mode amplitudes, see figure 12.

for the sum self-interaction (harmonic). The spanwise wavelength of these small-scale structures ($\lambda_z \approx 0.45$) is in good agreement with the distortions of the mean flow in figure 4(*c*) suggesting them to be stationary in nature.

The spanwise representation of the subharmonic and its nonlinear triadic interactions with itself, the fundamental (forced) mode and its harmonic and half-harmonics are shown for relevant interactions for the intermediate- and high-amplitude forcing (figure 18). Even in a 'quasi'-2-D flow, the subharmonic is usually the result of a pair of oblique modes of equal amplitude but opposite angle (Monkewitz 1988). The difference interaction of the two oblique modes readily explains the chequerboard pattern observed in figures 18(*a*) and 18(*b*). The spanwise wavelengths are $\lambda_z \approx 0.83$ (5 kVpp) and $\lambda_z \approx 0.81$ (7 kVpp), respectively. Further downstream, interactions of the subharmonic with the fundamental mode lead to patterns with smaller (half) streamwise wavelengths and similar spanwise wavelengths (figures 18*c* and 18*d*). In the case of intermediate forcing, the two interactions resulting in the half-harmonic at $f/f_{AFC} = 2.5$ appear at the same spanwise wavelength, albeit an even smaller streamwise wavelength (figures 18*e* and 18*f*). The prominent representations of the modes and their interactions, in particular in the intermediate forcing case, further corroborate the delayed breakdown to small scales, with only a few mode interactions for $24 < x = 26$. Early turbulent breakdown in the high forcing case leads to only weak and rather unorganised structures downstream of the LSB.

Comparisons of the mean flow distortion and the characteristic spanwise wavelength in the unsteady dynamics of the shear layer for the intermediate and high forcing amplitude are presented in figure 19. Mean flow contour lines are shown as an overlay on the interaction maps for the difference self-interaction of the subharmonic, representative of the spanwise periodicity in the wall-parallel measurements for all triadic interactions related to the subharmonic. The large spanwise wavelength of the mean flow deformation at intermediate forcing amplitudes does not show any notable relation to the spanwise wavelength of the dynamic interactions. The SPOD modes for different wall-normal locations for the fundamental mode of the K–H instability for the baseline ($f/f_{AFC} = 1.25$ in figure 7*a*) for different wall-normal locations (not shown here) show stronger spanwise modulation of the initially 2-D structures near the wall. Further away from the wall near

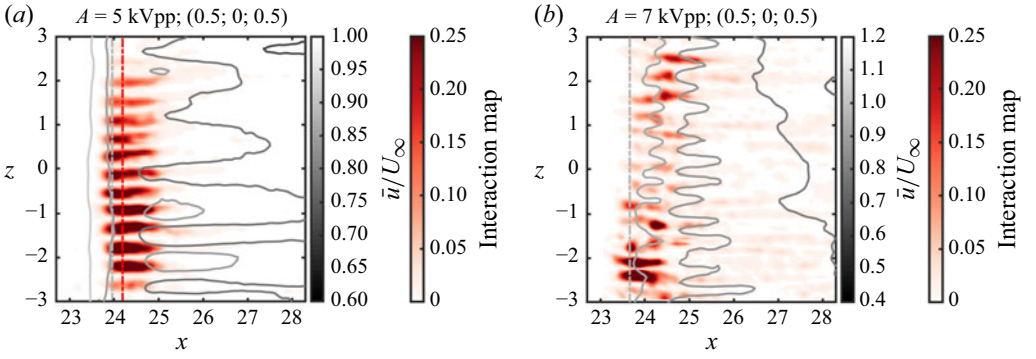

Figure 19. Mean flow overlay for the wall-parallel plane near the maximum displacement thickness and interaction maps of the difference self-interaction of the subharmonic ($f/f_{AFC} = 0.5$) with AFC.

the shear layer and towards the free stream the coherent structures show an increasingly higher degree of coherence along the span for the same streamwise locations. This is consistent with the BMD interaction maps in the centreline ([1.25; 0; 1.25] in figure 13*b*) and hints at the origin of the large-wavelength spanwise undulations inside the LSB. The AFC significantly increases the disturbance amplitude of the fundamental mode relative to the baseline case. The maximum reverse flow amplitude for the baseline case and the intermediate forcing amplitude of 5 kVpp – based on the centreline measurements – was found to be $7\,\% \leq u^*_{rev} \leq 11\,\%$ (relative to the free-stream velocity at separation $U_{\infty,s}$, $u^*_{rev} = u_{rev}/U_{\infty,s}$), which may be sufficient for the presence of an absolute instability (Rodriguez & Theofilis 2010; Hosseinverdi & Fasel 2013; Rodríguez *et al.* 2013; Embacher & Fasel 2014). Prior work (Borgmann *et al.* 2025) showed the presence of such an absolute instability for the baseline case (without the actuator present). At high forcing amplitudes, the reverse flow in the LSB is below 7 %. At high forcing amplitudes (7 kVpp) the wavelength of spanwise deformation of the mean flow agrees with the wavelength of the dynamics of the shear layer related to the subharmonic and half-harmonic at $f = 1.5\,f_{AFC}$ (SPOD and BMD [0.5; 0; 0.5] and [1; 0.5; 1.5]; figure 19*a*). This suggests that at high forcing amplitudes the shear-layer dynamics influences the mean flow. Stability calculations for the baseline and forced flow fields are necessary to determine the global and local stability of the forced flow, but this is beyond the scope of this work. Secondary instability analysis for the time-periodic base flow within the coherent vortices (Borgmann *et al.* 2022) found the dominant secondary instability at the subharmonic of the forced mode, consistent with this work. The corresponding spanwise wavelength was found at $\lambda_z \approx 1$ within the tested discrete wavelengths of $\lambda_z = [0.5, 1, 2]$ (with the actual value expected to be slightly lower if the resolution were to be increased). The most unstable mode showed a tendency towards larger wavelength for forcing amplitudes approaching the critical amplitudes (A_{cr}, necessary for a secondarily stable LSB). The dominant spanwise wavelength in the mean flow for the baseline in this work is in reasonable agreement with the stability calculations, while the larger wavelength in the intermediate forcing amplitude follows the expected trend. No stability calculations were available for comparison with the highest forcing amplitudes.

At higher forcing amplitudes the origin of the small-scale spanwise-periodic structures appears near the wall as well. The spanwise-coherent structures nearest to the wall are modulated, while on the high-speed side of the shear layer, away from the wall, the first few periods of the K–H mode remain largely unaffected and visual modulation only appears farther downstream (figure 7). Results in figure 19(*b*) relate the small-scale spanwise

undulations to the spanwise wavelength of the nonlinear interactions connected to the subharmonic. The spanwise wavelength of the interaction is identical to that observed in the mean flow at the highest forcing amplitudes. This implies that for sufficient forcing amplitudes, the spanwise deformation of the mean flow is a result of the disturbances in the shear layer. In this case, the interaction of two oblique subharmonic modes leads to a steady interference pattern in the flow.

5. Summary and conclusion

The response of LSBs to periodic 2-D disturbance input at moderate to high forcing amplitudes is investigated experimentally. The LSB in this work is generated by the favourable to adverse pressure gradient under a high-aspect-ratio ($L_{z,WT}/c = 6$, where $L_{z,WT}$ is the width of the model in the wind tunnel) inverted modified NACA 64_3-618 airfoil at $Re_C = 90\,000$. Two-dimensional periodic disturbances are generated by an ac-DBD plasma actuator located near the onset of the adverse pressure gradient. The effect of excitation amplitude to the amplitude development of the K–H instability in the shear layer and the impact on the transition process are examined using time-resolved PIV measurements along the centreline and several wall-parallel planes. Time-averaged measurements along the centreline show the expected effect on the bubble size, with a progressively smaller LSB as the forcing amplitude is increased. Three-dimensional reconstruction of the time-averaged flow fields, however, shows significant spanwise periodic deformation of the mean flow at different spanwise wavelength seemingly dependent on the forcing amplitudes. Spectral analysis of the velocity signal and modal decomposition of the flow field confirm that periodic excitation leads to higher amplitudes of the 2-D coherent roller structures than in the unforced case, resulting from the disturbance growth due to the K–H instability in the separated shear layer. Largest amplitudes and highest levels of coherence are observed for intermediate forcing amplitudes, suggesting the existence of an optimal forcing level to generate strong 2-D rollers. High-amplitude forcing led to smaller growth rates of the K–H mode in the LSB and earlier saturation at lower finite amplitudes, suggesting earlier onset of nonlinear interactions. Time traces and spectral analysis confirm the early breakdown of periodic structures in the flow at high-amplitude forcing, while at intermediate forcing the amplitudes of the forced mode and the periodicity of the velocity signal remain high at significant lengths downstream ($x = 26$, $\approx \Delta L_{b,5\,\mathrm{kVpp}}$ downstream of reattachment). These results suggest that the transition at intermediate forcing amplitudes, in particular at 5 kVpp, is delayed to a location downstream of reattachment. The strong spanwise-coherent vortical structures appear sufficient to reattach the flow, prior to breakdown to turbulence, similar to the direct numerical simulation results by Hosseinverdi & Fasel (2018). Modal analysis finds that periodicity in the spanwise modulation of the mean flow at high-amplitude forcing agrees with the wavelength of a subharmonic mode growing downstream of the initial saturation of the forced mode. The results suggest that the mean flow modulation at high amplitudes is a direct result of the forcing and possibly an interaction of two oblique subharmonic modes. The subharmonic modes appear as a result of the forced 2-D mode. The dominant spanwise wavelength at intermediate forcing amplitudes does not show a direct relation to the unsteady dynamics in the shear layer. The spanwise wavelength of the subharmonic interaction in the LSB is significantly smaller than the observed mean flow deformation. The results in this work agree with the numerical calculations in Hosseinverdi & Fasel (2018), showing a critical forcing amplitude to the amplification of the 2-D mode and potential delay of transition. Below such critical amplitudes, the developing vortical structures are not strong enough

to overcome the global instability in the LSB. At supercritical forcing amplitudes, the early onset of nonlinear interactions leads to rapid breakdown and turbulent reattachment. Overall, results corroborate direct numerical simulation findings by Hosseinverdi & Fasel (2018) and point to the existence of an optimal forcing amplitude for control of transition in LSBs in the presence of FST.

Acknowledgements. The authors would like to thank Dr S. Hosseinverdi for his continuous support through numerical simulations and insightful discussions throughout the project.

Funding. This work was supported by the National Science Foundation (NSF) under grant number 1805273, with Dr R. Joslin serving as the programme manager.

Declaration of interests. The authors report no conflict of interest.

References

ADRIAN, R. J. & WESTERWEEL, J. 2011 *Particle Image Velocimetry*. Cambridge University Press.

AGATE, M., PANDE, A., LITTLE, J. C., GROSS, A. & FASEL, H. F. 2018 Active flow control of the laminar separation bubble on an oscillating airfoil near stall. In *2018 AIAA Aerospace Sciences Meeting*, pp. 2049. American Institute of Aeronautics and Astronautics (AIAA).

ALAM, M. & SANDHAM, N. D. 2000 Direct numerical simulation of 'short' laminar separation bubbles with turbulent reattachment. *J. Fluid Mech.* **410**, 1–28.

BAKE, S., MEYER, D. G. W. & RIST, U. 2002 Turbulence mechanism in Klebanoff transition: a quantitative comparison of experiment and direct numerical simulation. *J. Fluid Mech.* **459**, 217–243.

BALZER, W. & FASEL, H. F. 2016 Numerical investigation of the role of free-stream turbulence in boundary-layer separation. *J. Fluid Mech.* **801**, 289–321.

BENARD, N. & MOREAU, E. 2014 Electrical and mechanical characteristics of surface AC dielectric barrier discharge plasma actuators applied to airflow control. *Exp. Fluids* **55** (11), 1–43.

BENTON, S. I. & VISBAL, M. 2016 Investigation of high-frequency separation control mechanisms for delay of unsteady separation. In *8th AIAA Flow Control Conference*, pp. 1–25. American Institute of Aeronautics and Astronautics.

BENTON, S. I. & VISBAL, M. R. 2018 High-frequency forcing to mitigate unsteady separation from a bursting separation bubble. *Phys. Rev. Fluids* **3** (1), 013907.

BORGMANN, D., HOSSEINVERDI, S., LITTLE, J. & FASEL, H. 2025 Experimental and numerical investigations of transition in a pressure-gradient-induced laminar separation bubble. *J. Fluid Mech.* **1007**, A23.

BORGMANN, D., HOSSEINVERDI, S., LITTLE, J. C. & FASEL, H. F. 2020 Investigation of low-speed boundary-layer instability and transition using experiments, theory and dns. In *AIAA AVIATION. 2020 FORUM*, pp. 2948. American Institute of Aeronautics and Astronautics (AIAA).

BORGMANN, D., HOSSEINVERDI, S., LITTLE, J. C. & FASEL, H. F. 2021 Investigation of laminar separation bubbles using experiments, theory and DNS. In *AIAA Aviation 2021 Forum*, pp. 2898. American Institute of Aeronautics and Astronautics (AIAA).

BORGMANN, D., HOSSEINVERDI, S., LITTLE, J. C. & FASEL, H. F. 2022 Active control of boundary-layer transition in laminar separation bubbles. In *AIAA SCITECH. 2022 Forum*, pp. 2433. American Institute of Aeronautics and Astronautics (AIAA).

CORKE, T. C., ENLOE, C. L. & WILKINSON, S. P. 2010 Dielectric barrier discharge plasma actuators for flow control. *Annu. Rev. Fluid Mech.* **42** (1), 505–529.

DIWAN, S. S. & RAMESH, O. N. 2009 On the origin of the inflectional instability of a laminar separation bubble. *J. Fluid Mech.* **629**, 263–298.

EMBACHER, M. & FASEL, H. F. 2014 Direct numerical simulations of laminar separation bubbles: investigation of absolute instability and active flow control of transition to turbulence. *J. Fluid Mech.* **747**, 141–185.

FASEL, H. F. 2002 Numerical investigation of the interaction of the Klebanoff-mode with a Tollmien–Schlichting wave. *J. Fluid Mech.* **450**, 1–33.

GASTER, M. 1967 The structure and behaviour of laminar separation bubbles, vol. 3595, pp. 1–31. Aeronautical Research Council Reports and Memoranda.

GEORGE, W. K., BEUTHER, P. D. & LUMLEY, J. L. 1978 Processing of random signals. In *Proceedings of the Dynamic Flow Conference 1978 on Dynamic Measurements in Unsteady Flows*, pp. 757–800. Springer.

GRAFTIEAUX, L., MICHARD, M. & GROSJEAN, N. 2001 Combining piv, pod and vortex identification algorithms for the study of unsteady turbulent swirling flows. *Meas. Sci. Technol.* **12** (9), 1422–1429.
GREENBLATT, D. & WYGNANSKI, I. J. 2000 The control of flow separation by periodic excitation. *Prog. Aerosp. Sci.* **36** (7), 487–545.
GROSS, A., LITTLE, J. & FASEL, H. 2017 Numerical simulation of wing section undergoing plunging motions at high angles of attack. In *47th AIAA Fluid Dynamics Conference,* pp. 3321. American Institute of Aeronautics and Astronautics (AIAA).
HÄGGMARK, C. P., HILDINGS, C. & HENNINGSON, D. S. 2001 A numerical and experimental study of a transitional separation bubble. *Aerosp. Sci. Technol.* **5** (5), 317–328.
HAIN, R., KÄHLER, C. J. & RADESPIEL, R. 2009 Dynamics of laminar separation bubbles at low-Reynolds-number aerofoils. *J. Fluid Mech.* **630**, 129–153.
HO, C. M. & HUERRE, P. 1984 Perturbed free shear layers. *Annu. Rev. Fluid Mech.* **16** (1), 365–422.
HORN, R. A. & JOHNSON, C. R. 1994 *Topics in Matrix Analysis*. Cambridge University Press.
HORTON, H. P. 1968 Laminar separation bubbles in two and three dimensional incompressible flow. PhD thesis, Queen Mary University of London, UK.
HOSSEINVERDI, S. & FASEL, H. 2013 Direct numerical simulations of transition to turbulence in two-dimensional laminar separation bubbles. In *51st AIAA Aerospace Sciences Meeting including the New Horizons Forum and Aerospace Exposition*, pp. 264. American Institute of Aeronautics and Astronautics (AIAA).
HOSSEINVERDI, S. & FASEL, H. F. 2017 Numerical investigation of the interaction of active flow control and Klebanoff modes. In *47th AIAA Fluid Dynamics Conference*, pp. 1–17. American Institute of Aeronautics and Astronautics.
HOSSEINVERDI, S. & FASEL, H. F. 2018 Role of Klebanoff modes in active flow control of separation: direct numerical simulations. *J. Fluid Mech.* **850**, 954–983.
HOSSEINVERDI, S. & FASEL, H. F. 2019 Numerical investigation of laminar–turbulent transition in laminar separation bubbles: the effect of free-stream turbulence. *J. Fluid Mech.* **858**, 714–759.
HUSAIN, H. S. & HUSSAIN, F. 1995 Experiments on subharmonic resonance in a shear layer. *J. Fluid Mech.* **304**, 343–372.
ISTVAN, M. S. & YARUSEVYCH, S. 2018 Effects of free-stream turbulence intensity on transition in a laminar separation bubble formed over an airfoil. *Exp. Fluids* **59** (3), 1–21.
JACOBS, R. G. & DURBIN, P. A. 2001 Simulations of bypass transition. *J. Fluid Mech.* **428**, 185–212.
JAROSLAWSKI, T., FORTE, M., VERMEERSCH, O., MOSCHETTA, J.-M. & GOWREE, E. R. 2023 Disturbance growth in a laminar separation bubble subjected to free-stream turbulence. *J. Fluid Mech.* **956**, A33.
JONES, L. E., SANDBERG, R. D. & SANDHAM, N. D. 2008 Direct numerical simulations of forced and unforced separation bubbles on an airfoil at incidence. *J. Fluid Mech.* **602**, 175–207.
KENDALL, J. 1985 Experimental study of disturbances produced in a pre-transitional laminar boundary layer by weak freestream turbulence. In *18th Fluid Dynamics and Plasmadynamics and Lasers Conference*, pp. 1695. American Institute of Aeronautics and Astronautics (AIAA).
KLEBANOFF, P. S. 1971 Effect of free-stream turbulence on a laminar boundary layer. *Bull. Am. Phys. Soc.* **16**, 1323+.
KLEBANOFF, P. S., TIDSTROM, K. D. & SARGENT, L. M. 1962 The three-dimensional nature of boundary-layer instability. *J. Fluid Mech.* **12** (1), 1–34.
KOTSONIS, M. 2015 Diagnostics for characterisation of plasma actuators. *Meas. Sci. Technol.* **26** (9), 092001.
KOTSONIS, M., GHAEMI, S., VELDHUIS, L. & SCARANO, F. 2011 Measurement of the body force field of plasma actuators. *J. Phys. D: Appl. Phys.* **44** (4), 045204.
KURELEK, J. W., KOTSONIS, M. & YARUSEVYCH, S. 2018 Transition in a separation bubble under tonal and broadband acoustic excitation. *J. Fluid Mech.* **853**, 1–36.
KURELEK, J. W., TUNA, B. A., YARUSEVYCH, S. & KOTSONIS, M. 2020 Three-dimensional development of coherent structures in a two-dimensional laminar separation bubble. *AIAA J.* **59** (2), 1–13.
LIN, N., REED, H.L. & SARIC, W. S. 1992 Effect of leading-edge geometry on boundary-layer receptivity to freestream sound. In *Instability, Transition, and Turbulence*, pp. 421–440. Springer.
LITTLE, J., SINGH, A., ASHCRAFT, T. & DURASIEWICZ, C. 2019 Post-stall flow control using nanosecond pulse driven dielectric barrier discharge plasma actuators. *Plasma Sour. Sci. Technol.* **28** (1), 014002.
MADEN, I., MADUTA, R., KRIEGSEIS, J., JAKIRLIĆ, S., SCHWARZ, C., GRUNDMANN, S. & TROPEA, C. 2013 Experimental and computational study of the flow induced by a plasma actuator. *Intl J. Heat Fluid Flow* **41**, 80–89.
MALMIR, F., DI LABBIO, G., LE FLOC'H, A., DUFRESNE, L., WEISS, J. & VÉTEL, J. 2024 Low-frequency unsteadiness in laminar separation bubbles. *J. Fluid Mech.* **999**, A99.

MARXEN, O. & HENNINGSON, D.S. 2011 The effect of small-amplitude convective disturbances on the size and bursting of a laminar separation bubble. *J. Fluid Mech.* **671**, 1–33.
MARXEN, O., LANG, M. & RIST, U. 2012 Discrete linear local eigenmodes in a separating laminar boundary layer. *J. Fluid Mech.* **711**, 1–26.
MARXEN, O., LANG, M. & RIST, U. 2013 Vortex formation and vortex breakup in a laminar separation bubble. *J. Fluid Mech.* **728**, 58–90.
MARXEN, O., LANG, M., RIST, U., LEVIN, O. & HENNINGSON, D. S. 2009 Mechanisms for spatial steady three-dimensional disturbance growth in a non-parallel and separating boundary layer. *J. Fluid Mech.* **634**, 165–189.
MARXEN, O., LANG, M., RIST, U. & WAGNER, S. 2003 A combined experimental/numerical study of unsteady phenomena in a laminar separation bubble. *Flow Turbul. Combust.* **71** (1-4), 133–146.
MAUCHER, U., RIST, U. & WAGNER, S. 2000 Secondary disturbance amplification and transition in laminar separation bubbles. In *Laminar-Turbulent Transition: IUTAM Symposium, Sedona/AZ September 13–17, 1999*, pp. 657–662. Springer.
MICHELIS, T., YARUSEVYCH, S. & KOTSONIS, M. 2017 Response of a laminar separation bubble to impulsive forcing. *J. Fluid Mech.* **820**, 633–666.
MICHELIS, T., YARUSEVYCH, S. & KOTSONIS, M. 2018 On the origin of spanwise vortex deformations in laminar separation bubbles. *J. Fluid Mech.* **841**, 81–108.
MONKEWITZ, P. A. 1988 Subharmonic resonance, pairing and shredding in the mixing layer. *J. Fluid Mech.* **188**, 223–252.
MORKOVIN, M. V. 1969 On the many faces of transition. In *Viscous Drag Reduction: Proceedings of the Symposium on Viscous Drag Reduction held at the LTV Research Center, Dallas, Texas, September 24 and 25, 1968*,pp. 1–31. Springer.
POSTL, D., BALZER, W. & FASEL, H. F. 2011 Control of laminar separation using pulsed vortex generator jets: direct numerical simulations. *J. Fluid Mech.* **676**, 81–109.
RIST, U. & MAUCHER, U. 1994 Direct numerical simulation of 2-D and 3-D instability waves in a laminar separation bubble. In *AGard Conference Proceedings AGARD CP*, pp. 34–34. AGARD.
RODRÍGUEZ, D., GENNARO, E. M. & SOUZA, L. F. 2021 Self-excited primary and secondary instability of laminar separation bubbles. *J. Fluid Mech.* **906**, A13.
RODRÍGUEZ, D., GENNARO, E. M. & JUNIPER, M. P. 2013 The two classes of primary modal instability in laminar separation bubbles. *J. Fluid Mech.* **734**, R4.
RODRIGUEZ, D. & THEOFILIS, V. 2010 Structural changes of laminar separation bubbles induced by global linear instability. *J. Fluid Mech.* **655**, 280–305.
SCHMIDT, O. T. 2020 Bispectral mode decomposition of nonlinear flows. *Nonlinear Dyn.* **102** (4), 2479–2501.
SCHMIDT, O. T. & COLONIUS, T. 2020 Guide to spectral proper orthogonal decomposition. *AIAA J.* **58** (3), 1023–1033.
SIMONI, D., LENGANI, D., UBALDI, M., ZUNINO, P. & DELLACASAGRANDE, M. 2017 Inspection of the dynamic properties of laminar separation bubbles: free-stream turbulence intensity effects for different Reynolds numbers. *Exp. Fluids* **58** (6), 1–14.
SIMONI, D., UBALDI, M. & ZUNINO, P. 2014 Experimental investigation of flow instabilities in a laminar separation bubble. *J. Therm. Sci.* **23** (3), 203–214.
SINGH, N. K. 2019 Instability and transition in a laminar separation bubble. *J. Appl. Fluid Mech.* **12** (5), 1511–1525.
SIROVICH, L. 1987 Turbulence and the dynamics of coherent structures. I. Coherent structures. *Q. Appl. Maths* **45** (3), 561–571.
SPALART, P. R. & STRELETS, M. K. 2000 Mechanisms of transition and heat transfer in a separation bubble. *J. Fluid Mech.* **403**, 329–349.
THEOFILIS, V. 2011 Global linear instability. *Annu. Rev. Fluid Mech.* **43** (1), 319–352.
TOWNE, A., SCHMIDT, O. T. & COLONIUS, T. 2018 Spectral proper orthogonal decomposition and its relationship to dynamic mode decomposition and resolvent analysis. *J. Fluid Mech.* **847**, 821–867.
WATMUFF, J. H. 1999 Evolution of a wave packet into vortex loops in a laminar separation bubble. *J. Fluid Mech.* **397**, 119–169.
WATSON, G. A. 1996 Computing the numerical radius. *Linear Algebr. Applics.* **234**, 163–172.
WEINGAERTNER, A., TEWES, P. & LITTLE, J. C. 2020 Parallel vortex body interaction enabled by active flow control. *Exp. Fluids* **61** (6), 1–18.
WEISS, J., LITTLE, J. C., THREADGILL, J. A. & GROSS, A. 2021 Low-frequency unsteadiness in pressure-induced separation bubbles. In *AIAA SciTech 2021 Forum*, pp. 1324. American Institute of Aeronautics and Astronautics (AIAA).
WELCH, P. 1967 The use of fast fourier transform for the estimation of power spectra: a method based on time averaging over short, modified periodograms. *IEEE Trans. Audio Electroacoust.* **15** (2), 70–73.

WIENEKE, B. F. A. 2017 Piv uncertainty quantification and beyond. PhD thesis, Delft University of Technology, The Netherlands.

WOSZIDLO, R. & LITTLE, J. C. 2021 Recommended practices for characterization and documentation of active flow control actuators. In *AIAA Scitech 2021 Forum*, pp. 2002. American Institute of Aeronautics and Astronautics (AIAA).

YARUSEVYCH, S. & KOTSONIS, M. 2017 Steady and transient response of a laminar separation bubble to controlled disturbances. *J. Fluid Mech.* **813**, 955–990.

YEH, C.-A., BENTON, S.I., TAIRA, K., GARMANN, D.J. 2020 Resolvent analysis of an airfoil laminar separation bubble at Re = 5 00 000. *Phys. Rev. Fluids* **5** (8), 083906.